Review Article

ADVANCED PHOTONICS NEXUS

Metamaterial-enhanced magnetic resonance imaging: a review

Zhiwei Guo,*,† Yang Xu,† Shengyu Hu, Yuqian Wang, Yong Sun,* and Hong Chen*
Tongji University, School of Physics Science and Engineering, MOE, Key Laboratory of Advanced Micro-Structure Materials, Shanghai, China

Abstract. Magnetic resonance imaging (MRI), as a noninvasive and powerful method in modern diagnostics, has been advancing in leaps and bounds. Conventional methods to improve MRI based on increasing the static magnetic field strength are restricted by safety concerns, cost issues, and the impact on patient experience; as such, innovative approaches are required. It has been suggested that metamaterials featuring subwavelength unit cells can be used to take full control of electromagnetic waves and redistribute electromagnetic fields, achieve abundant counterintuitive phenomena, and construct versatile devices. Recently, metamaterials with exotic effective electromagnetic parameters, peculiar dispersion relations, or tailored field distribution of resonant modes have shown promising capabilities in MRI. Herein, we outline the principle of the MRI process, review recent advances in enhancing MRI by employing the unique physical mechanisms of metamaterials, and demystify ways in which metamaterial designs could improve MRI, such as by enhancing the imaging quality, reducing the scanning time, alleviating field inhomogeneities, and increasing patient safety. We conclude by providing our vision for the future of improving MRI with metamaterials.

Keywords: metamaterials; magnetic resonance imaging; radio-frequency magnetic field; effective parameters; dispersion relations; resonant modes.

Received Mar. 15, 2024; revised manuscript received Apr. 16, 2024; accepted for publication Jul. 22, 2024; published online Aug. 19, 2024.

[DOI: 10.1117/1.APN.3.5.054001]

1 Introduction

Magnetic resonance imaging (MRI) uses the magnetic resonance phenomenon, which was discovered by Edward Purcell and Felix Bloch in 1946.[1,2] Since then, research in this field has led to the award of several Nobel Prizes.[3] The first practical application of MRI dates back to 1973, when Lauterbur conducted an experiment on two tubes of distilled water.[4] In the decades since, MRI has advanced from a method used in a few specialized physical laboratories to a widely accepted approach of examination. As a mainstay among imaging tools in modern healthcare, MRI not only has profoundly affected the development of medical imaging[5,6] but also now plays a crucial role in biology,[7,8] chemistry,[9,10] physics,[11,12] and many other fields. MRI does not use ionizing radiation, it is non-invasive and generally safe, and it has the advantages of high contrast and high resolution; as such, it has unique superiority when compared to other imaging techniques.[13] Simply modifying the scanning parameters can achieve an arbitrary selection of imaging slices, provide different types of image contrast, and detect various components.

Taking advantage of substantial advances in information technology, electronics, and materials science, the imaging quality and application range of MRI has continued to increase, leading to myriad new methods, such as diffusion MRI,[14,15] high-resolution MRI,[16,17] and functional MRI.[18,19] However, these new methods present additional problems and challenges, requiring more innovative mechanisms.

The most straightforward way to enhance MRI is to increase the strength of the main magnetic field.[20] This can multiply the signal-to-noise ratio (SNR), boost sensitivity, and improve spatial and temporal resolution; however, it may also cause interference effects, present safety concerns, and increase costs. Some other approaches, including coil optimization,[21,22]

*Address all correspondence to Zhiwei Guo, 2014guozhiwei@tongji.edu.cn; Yong Sun, yongsun@tongji.edu.cn; Hong Chen, hongchen@tongji.edu.cn

†These authors contributed equally to this work.

pulse-sequence innovations,[23,24] imaging-algorithm improvements,[25,26] contrast agents,[27,28] or the use of dielectric materials[29,30] and dielectric resonators,[31,32] can improve MRI without changing the main magnetic field, and these techniques have been widely employed.

Metamaterials are artificial media composed of periodically arranged subwavelength unit cells;[33,34] they possess exotic electromagnetic properties that cannot be found in natural materials. The advent of metamaterials has opened new avenues for improving MRI, as summarized in Fig. 1. The possibility for on-demand design of metamaterials presents an abundant parametric space (including tunable effective permittivity, effective permeability, chirality, etc.), which in turn endows them with the powerful ability to arbitrarily affect electromagnetic waves. Their potential has been demonstrated in a host of applications, including electromagnetic cloaking,[41,42] perfect absorbers,[43,44] and subwavelength imaging.[45,46] Metasurfaces, the two-dimensional (2D) counterparts of metamaterials,[47] have also aroused great interest because of their compact, low-loss structures, and rich capacity for manipulation of electromagnetic waves.[48,49] For simplicity, we refer to both collectively as metamaterials. Metamaterials have recently come to the fore in MRI, and we have every reason to believe that this is just a promising beginning.

To the best of our knowledge, there has not yet been a review dedicated to the use of metamaterials for improving MRI, and

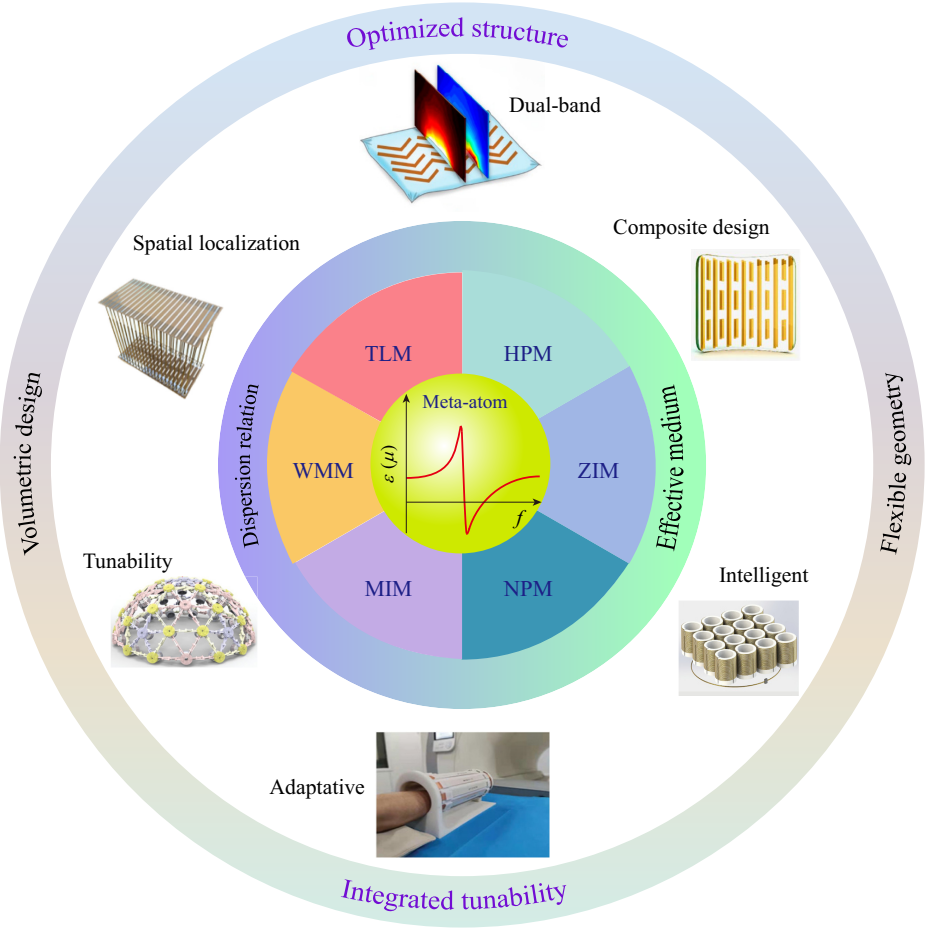

Fig. 1 Main directions and typical advances achieved by metamaterials to improve MRI. Three key aspects discussed in this review are metamaterials with exotic effective electromagnetic parameters [including negative-permeability metamaterials (NPMs), high-permeability/permittivity metamaterials (HPMs), and zero-index metamaterials (ZIMs)], metamaterials with peculiar dispersion relations [including magneto-inductive metamaterials (MIMs), wire-medium metamaterials (WMMs), and composed right-/left-handed transmission line metamaterials (TLMs)], and metamaterial resonators with tailored electromagnetic field distributions. There are two fundamental types of metamaterial resonators: those using optimized structures possessing different characteristics (e.g., flexible geometry, dual-band response, and volumetric arrangement) and those with integrated tunability and/or nonlinearity, featuring intelligence, adaptivity, or auxeticity. The figures are reproduced with permission from Ref. 35 © 2017 Springer Nature, licensed under a CC-BY 4.0 International License; Ref. 36 © 2017 American Chemical Society, licensed under a CC-BY-ND 4.0 License; Ref. 37 © 2018 Wiley-VCH; Ref. 38 © 2021 Wiley-VCH; Ref. 39 © 2021 Wiley-VCH; and Ref. 40 © 2019 Wiley-VCH.

the topic has only been discussed as part of broader reviews.[50,51] In this review, we first briefly introduce the principles of MRI to better illustrate how metamaterials can affect its imaging process. Then, we classify recent advances in metamaterials in MRI and attempt to clarify the routes by which they improve MRI based on specific physical mechanisms. Finally, we conclude by summarizing state of the art in the development of these techniques and present prospects for future research directions. We anticipate that this review will be useful to researchers who are interested in this topic.

2 Operation Principle of MRI Systems

The procedure for MRI can be simply divided into two steps: generating a nuclear magnetic resonance (NMR) signal from a sample and obtaining an image from this signal. We will now consider the first of these steps and the three types of magnetic fields involved. To better comprehend the magnetic resonance (MR) phenomenon, one may also revisit electron paramagnetic resonance, which works in a similar way.[52]

The first magnetic field is a static external magnetic field of the order of tesla (T), termed B_0, which enables the macroscopic magnetization of a sample. We take the most commonly used $^1_1$H nucleus as an example. These nuclei are easily magnetized and are widely found in biological tissues; most importantly, they have a nonzero spin quantum number and thus exhibit a magnetic moment. Nonetheless, the magnetic moments of large collections of hydrogen nuclei will generally be randomly orientated, without a net magnetization vector (NMV), as shown in Fig. 2(a). As shown in Fig. 2(b), once the static external magnetic field B_0 is applied, the nuclei tend to align in its direction (from the perspective of quantum theory, it is interpreted that more nuclei will reside in the lower of two splitting energy levels[53]). A macroscopic magnetization vector M is then obtained with a direction the same as B_0 but with a far lower strength, meaning it is still undetectable. Moreover, since the orientation of the magnetic moment and the torque are not exactly parallel, the nuclei will precess around B_0 with the Larmor frequency,

$$\omega_0 = \gamma B_0, \tag{1}$$

where γ denotes the gyromagnetic ratio, which is related to the specific charge and Landé g-factor of the nucleus. For the hydrogen nucleus, this quantity is 42.57 MHz/T, which determines its Larmor frequency at different field strengths.

The second magnetic field is a radio-frequency (RF) magnetic field of the order of μT that is perpendicular to B_0, termed B_1. This serves to excite the nuclei and make the NMV detectable. The applied RF pulse is generally linearly or circularly polarized and has the same frequency as that of nuclear precession; some nuclei will thus absorb energy via resonance. We now temporarily turn to a rotating reference frame whose

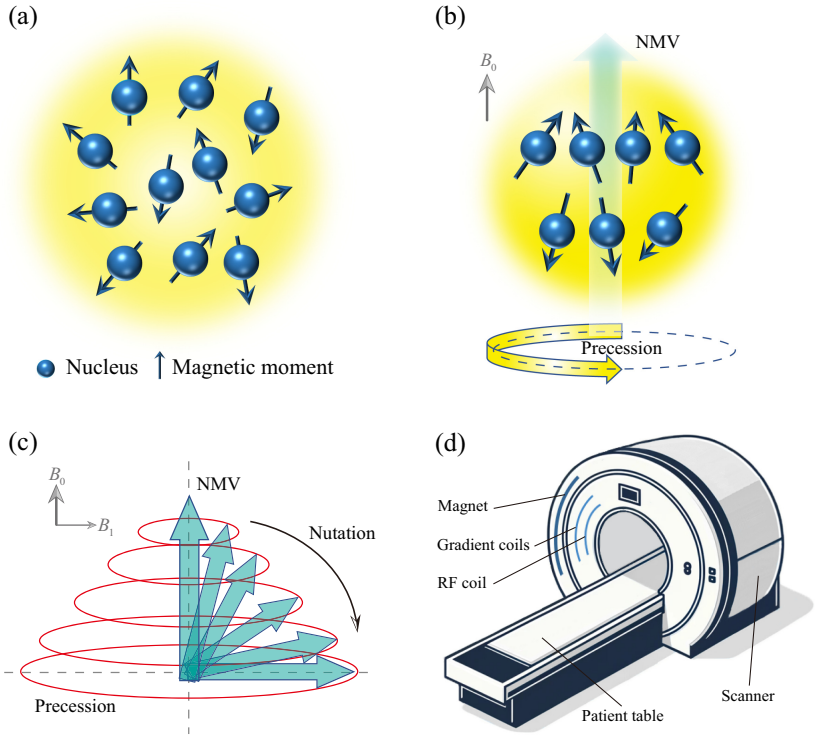

Fig. 2 Principle of MRI. (a) Several nuclei are randomly orientated, thus exhibiting zero NMV. (b) After the introduction of the static external magnetic field B_0, more nuclei tend to align in the direction of B_0, contributing to a nonzero NMV. Inexactly aligned magnetic moments will precess around B_0, as will the NMV. (c) The RF magnetic field B_1 can cause the NMV to flip into the transverse direction and become detectable. The flip angle (FA) is dependent on the strength and duration of B_1. (d) Schematic of an open MRI machine. The shaded arcs indicate the radial positions of different components integrated within the scanner.

direction and frequency are equal to those of nucleus precession.[54] In this frame, the nuclei are motionless, and things become the same. Due to the nonzero angle between the direction of the magnetic moment and the RF magnetic field, the magnetic moments of the nuclei will precess around B_1. Back in the laboratory reference frame, the result is that the NMV exhibits quick precession and slow nutation simultaneously, as shown in Fig. 2(c). The FA of M has a dependence on the excitation field strength B_1 and the pulse duration time per period τ,

$$\theta = \gamma B_1 \tau. \tag{2}$$

Upon the removal of the RF pulse, the nuclei release their absorbed energy and generate an electromagnetic induction signal that can be picked up by coils. The signal intensity and the relaxation time of magnetization-vector recovery can be used to discriminate different components or tissues.[55]

The third magnetic field is a quasi-static gradient field of the order of mT; this is a modification of the initial homogeneous static field to achieve spatial positioning. It is necessary to distinguish different locations in the whole imaging area for overall diagnosis or analysis. The gradient field consists of three static magnetic fields varying linearly along the x, y, and z directions. These have a slight rangeability and are applied at different times during the imaging process. The introduction of gradient fields leads to every point in space experiencing a unique static magnetic field. The nuclei will only be excited when their precession frequency at the field strength in their location is sufficiently close to the frequency of the applied RF magnetic field. Applying a gradient magnetic field is equivalent to encoding different voxels (the 3D counterparts of 2D pixels), and repeated RF pulses can then be used in a parameter-sweeping process to obtain information about every voxel.

The three kinds of magnetic fields described above, with their separate functionalities (alignment, excitation, and spatial localization), work together to lay an indispensable foundation for the imaging process. In Fig. 2(d), an open MRI machine with the main components is shown. The scanner contains the magnet, the gradient coils, the RF coil, and other elements, while the table supports the tested samples or patients. An MR signal is generated within the bore and collected by the receiver coil. The collected MR signal is recorded by a computer, and images are finally produced through signal-processing procedures, such as amplification, weighting, and spatial Fourier transforms. Detailed descriptions of these operations can be found elsewhere.[56,57]

For an MRI image, imaging sequences, weighted approaches, cutting slices, and other complicated settings, chosen in accordance with specific aims and tested regions, will affect the final result. Essentially, the inherent density of excited nuclei decides the obtained signal intensity (usually distinguished by the gray level) exhibited in the pictures under the same conditions. The intensity differences are compared to clinically judge the physical condition of patients. Therefore, one may qualitatively assess the MRI images in a preliminary manner by considering the contrasts between different positions, the resolution of tissues or organs, and the potential artifacts.

The SNR is a vital metric for quantitatively measuring the imaging quality in MRI. The SNR can be approximated using the following equation:[58,59]

$$\mathrm{SNR} \sim \frac{B_0^2 \sin(\gamma B_1^+ \tau) B_1^-}{\sqrt{R_{\mathrm{coil}} + R_{\mathrm{sample}}}}, \tag{3}$$

in which the quadratic term indicates that B_0 affects the energy-level difference and precession frequency, the sinusoidal term indicates that the FA determines the transverse projection of the NMV, B_1^+ is the transmitted magnetic field, B_1^- is the magnetic field that the receiver coil could generate if it served as a transmitter coil with a unit driving current (based on the principle of reciprocity[60]), and R_{coil} represents the resistance of the receiver coil, while R_{sample} represents the equivalent resistance of the sample to the coil. The dissipated power of the coil and the sample, which will inevitably contribute to the noise, is directly proportional to corresponding resistances. Specifically, the former attributes to the skin effect on the surface of the coil, while the latter occurs mainly due to the induced eddy currents within the conductive sample.[58]

With the rapid development of MRI technology, the possible strength of B_0 has steadily grown from a few tenths of a tesla to more than 20 T today.[61,62] Increasing B_0 can substantially boost the theoretical upper limit of the SNR, but this is accompanied by safety concerns, cost issues, and impacts on the patient experience. In parallel, at high fields, the RF wavelength becomes comparable to the dimensions of the sample, which may aggravate the wave behavior and degrade the imaging quality.[63] In view of the fact that these problems cannot be easily solved in the near term, mainstream clinical devices are still running at fields of the order of 3.0, 1.5 T, or even lower. According to Eq. (3), increasing B_1 may be an alternative solution. Metamaterials can manipulate the propagation path and spatial distribution of the RF magnetic field while barely disturbing the static magnetic field; however, the responses of most metamaterials involve a narrow frequency band, which is generally regarded as a drawback. Nonetheless, the bandwidth of the RF magnetic field in MRI is also limited; thus, metamaterials are naturally suited to improve MRI. Various applications of metamaterials in MRI are detailed in the subsequent sections.

3 Metamaterials with Extreme Electromagnetic Properties for MRI

3.1 Metamaterials with Extreme Electromagnetic Parameters

It has been suggested that a microstructure composed of periodically arranged components could produce novel electromagnetic responses.[33,34] In the subwavelength context, the macroscopic properties of these metamaterials can be described by effective electromagnetic parameters according to the effective medium theory.[64] By precise structure design, particular effective parameters and other relevant properties can be achieved at a specific frequency. The ability to exhibit artificial magnetism or dielectric property with nonmagnetic components renders this sort of material compatible with MRI equipment. Recent studies have demonstrated the potential for constructing metamaterials with extreme effective permeabilities or permittivities that could improve MRI by tailoring the propagation of electromagnetic waves.

3.1.1 High-permeability metamaterials as flux guides

In MRI, the transmission and reception process of the RF magnetic field rely on coils. Typical transmitter coils are volume

coils, such as birdcage coils[58] and transverse electromagnetic (TEM) coils.[65] When it comes to the receiver, volumetric coils can maintain uniformity, but local coils are often employed to ensure adequate SNR. Nevertheless, the signal accepted by a local coil will decay with the distance between it and the sample. To address this problem, a classical artificial magnetic material, the "Swiss roll" has been adopted.[66]

A diagram of the Swiss-roll structure is shown in Fig. 3(a). This is composed of a spiral made from several turns of a conductor with an insulating backing wound on a central mandrel. When an alternating magnetic field is applied, a current will be induced in the spiral, and this will begin to flow due to the distributed capacitance between the sheets. This leads to anisotropic magnetism in the Swiss roll as follows:[70]

$$\mu_{\parallel} = 1 - \frac{F}{\left(1 - \frac{\omega_0^2}{\omega^2}\right) + i\frac{\Gamma}{\omega}} \quad \text{and} \quad \mu_{\perp} = 1, \tag{4}$$

where F is the filling factor, ω_0 is the resonant frequency, and Γ is the loss. The filling factor F represents the fractional area of a unit cell occupied by the interior of Swiss rolls,[33] which is thus a frequency-independent amount only affecting the magnitude. Intriguingly, high permeability implies low reluctance, providing a route to reduce the RF magnetic flux leakage during transmission. Swiss rolls were designed that showed a permeability of 2.23 at 21.23 MHz, which is approximately the Larmor frequency at 0.5 T. Figures 3(b) and 3(c) present the results obtained from this MRI experiment. Notably, with the use of Swiss rolls, the RF magnetic flux carrying the image information of a thumb was ducted to a surface coil 20 cm away, and a clear image was obtained.

This pioneering research was the first employment of metamaterials in MRI. However, compared to the standard reference image, the image obtained with the use of Swiss rolls was not able to accurately conserve spatial information due to the length of the rolls, along with their low permeability and poor Q-factor.[67] The magnitude distribution and contours of an M-shaped antenna have been reproduced at the imaging end of the structure [see Figs. 3(d)–3(f)], assisted by a parameter-optimized Swiss-roll structure.[67,70] In addition, Swiss rolls shaped in a yoke while encircling the sample were proved to enhance the detection performance of the receiver coil.[71] These modified works further demonstrate that metamaterials with high effective permeability can serve as near-field transfer media.

3.1.2 Negative-permeability metamaterials as superlenses

Before the concept was greatly expanded, the term metamaterials referred to negative-index metamaterials (NIMs) with both negative permittivity and negative permeability. A variety of counterintuitive electromagnetic properties have been suggested for NIMs, such as negative refraction,[72] reversed Cherenkov effect,[73] reversed Doppler effect,[74] and superlensing.[75] It is known that an NIM superlens can amplify evanescent waves to achieve a perfect image beyond the limit of diffraction, albeit without the consideration of loss. This notion can also be used to guide the design of RF lenses in MRI. Unlike a conventional superlens, which requires a negative index, MRI operates in the quasi-static realm; therefore, an NPM should be sufficient. The split-ring resonator (SRR) is another framework that can be used to construct metamaterials with particular permeability. An SRR has an electromagnetic response that is like that of a Swiss roll, and it can be used to create isotropic artificial magnetic materials.[33]

One of the earliest demonstrations in this field was a negative-permeability lens composed of capacitively loaded SRRs (CLSRRs), aiming to effectively "shorten" the distance from the sample to the detector.[68,76] In this work, the rings were placed in a cubic lattice to form the lens, and the unit cell consisted of a basic SRR and a capacitor to tune the resonant frequency. From a lossless perspective, the amplification of the evanescent RF magnetic field in a NIM of thickness d can compensate for the attenuation within the propagation distance d. In other words, the field on one side of the lens is equivalent to the field $2d$ away.[72] This suggests sensitivity enhancement of the receiver coil if such a lens is inserted between a sample and a coil. Evidently, the SNR would be boosted as long as the noise introduced by the CLSRRs did not exceed the gain of the signal. Figures 3(g) and 3(h) explicitly demonstrate the capacity of this system to image a deeper area, which results in improved imaging quality for the region of interest (ROI).

Another elegant application of NPMs is to improve the field localization of parallel magnetic resonance imaging (pMRI).[77] In pMRI, using multiple surface coils can partially replace the spatial coding to reduce the image acquisition time.[78] Owing to the recovery of high-order Fourier components and the focus of the image realized by a negative-permeability lens, the desire to better discriminate the field of every independent coil can be well satisfied. However, the inherent loss of bulky material limits the increase of the peak SNR to some extent. Some even more compact 2D configurations, such as water-tunable spiral coils and Hilbert curve-based resonators, have been proposed and examined.[79,80] These are not only able to enhance the RF magnetic field but also suitable for practical applications because of their reduced footprint.

3.1.3 Infinite- or zero-permeability metamaterials as local modification

The abundant possible functions of artificial magnetic metamaterials in MRI are also revealed in the local redistribution of the RF magnetic field. Aside from their negative permeability, the diverse possible magnetic responses of SRRs are still to be explored. Figures 3(i)–3(k) show that metamaterials with infinite or zero permeability can reject or confine the RF magnetic field, respectively,[69] and this can be interpreted by considering the specific boundary conditions they cause. It is worth noting that these two kinds of response may distort the excitation field. One solution to this issue is to add a pair of crossed diodes (or other nonlinear elements) to each SRR, allowing the material to switch between unity permeability under a strong excitation field and abnormal permeability under a weak reception field. The introduction of nonlinearity is instructive for the subsequent design of metamaterials for use in MRI.

With precise design, slabs possessing infinite or zero permeability have been obtained by periodically arranging SRRs. A $\mu \to \infty$ slab has in fact been mimicked by high-permeability SRR arrays. Figure 3(k) shows the SNR distributions with and without a $\mu \to \infty$ slab. The increased brightness in proximity to the slab confirms the enhancement of SNR. Practically, a $\mu \to \infty$ slab can be regarded as an effective magnetic wall,[68] where the magnetic field has only normal components. Therefore, it may serve as a reflector to reduce the decay of the RF magnetic field away from the receiver coil. A $\mu = 0$ slab needs a different orientation when used in MRI, as shown in

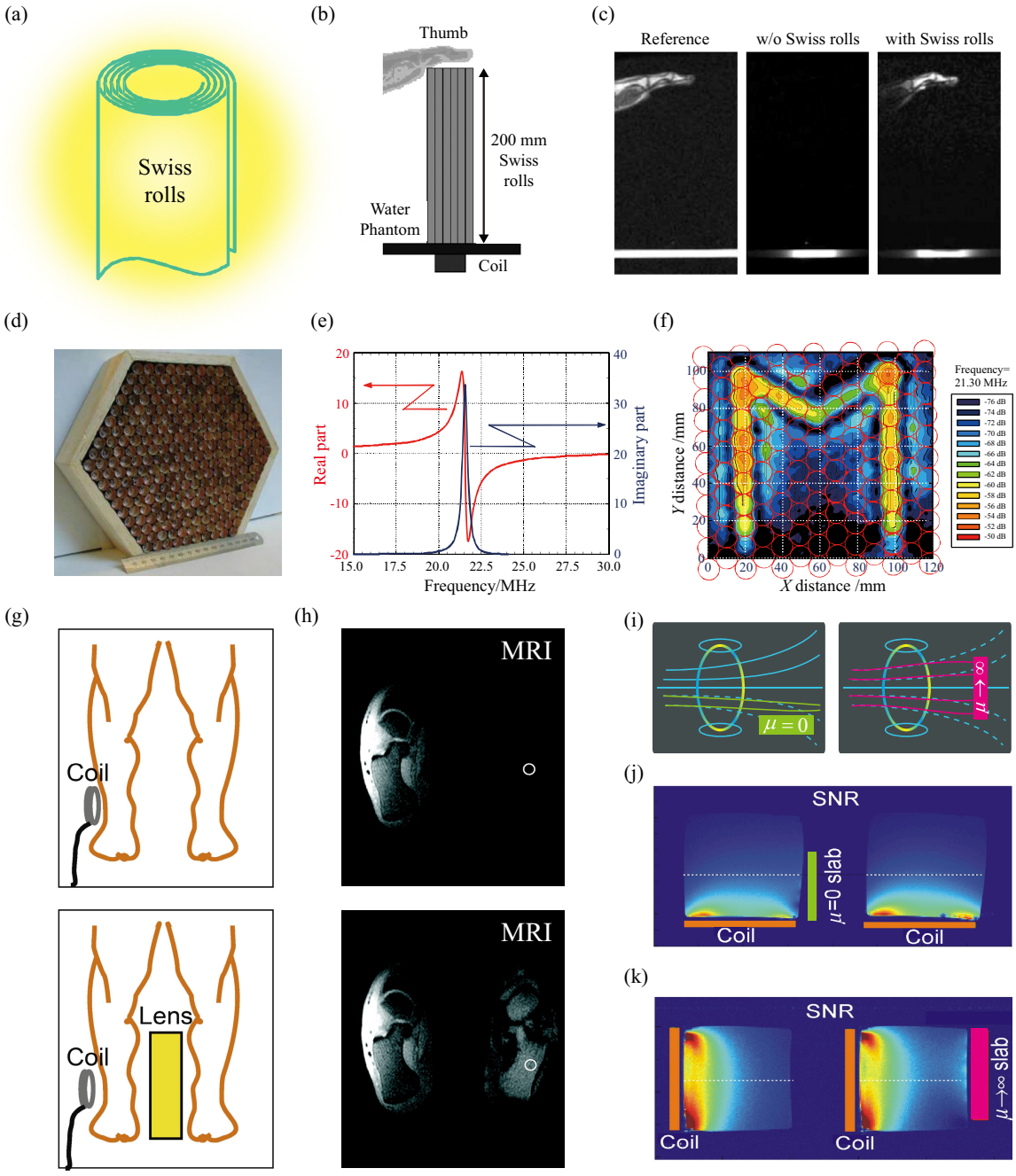

Fig. 3 Metamaterials with extreme electromagnetic parameters for MRI. (a) Schematic of a single Swiss roll. (b) Layout of the MRI imaging experiment. (c) 0.5-T MRI images of a thumb acquired for three cases: with the body coil in transceiver mode as a reference (left panel), and with a local coil as the receiver in the absence (middle panel) or presence of Swiss rolls (right panel). (d) Photograph of the M-shaped antenna. (e) Effective permeability as the function of frequency. (f) The field pattern observed above the parameter-optimized Swiss rolls (outlined in red). (g) Sketch of the experimental setup for the NPM lens and (h) obtained 1.5-T MRI images with and without the $\mu = -1$ metamaterial lens between two ankles. The SNR in the ROI indicated by a circle was increased by 2.6 times in the presence of the lens realized by NPMs. (i) Sketch of the magnetic-induction lines for a single coil with a $\mu = 0$ slab (left panel) and with a $\mu \to \infty$ slab (right panel). SNR maps measured by a 1.5-T receiver coil with and without (j) the $\mu = 0$ slab perpendicular to the coil or (k) the $\mu \to \infty$ slab parallel to the coil. The figures are reproduced with permission from (a)–(c) Ref. 66 © 2001 AAAS, (d)–(f) Ref. 67 © 2003 Optica, (g) and (h) Ref. 68 © 2010 Elsevier, and (j) and (k) Ref. 69 © 2011 American Institute of Physics (AIP).

Fig. 3(j); it acts as an extra border and limits the outward leakage of RF magnetic flux, contributing to enhancement of the SNR in the adjacent region. A combination of several slabs can be used to take full advantage of local magnetic field modification and improve imaging quality.

3.1.4 High-permittivity metamaterials as RF shimming

In high-field MRI, the standing wave effect may result in artifacts and deteriorate the imaging quality.[63] One possible solution is the employment of dielectric pads (DPs) as RF shimming.[81,82] The underlying mechanism is that the induced displacement currents can serve as a second magnetic field source, thus locally modifying the transmitted field and improving the inhomogeneity.[29] However, conventional DPs are formed by aqueous suspensions of metal titanates with high permittivity, whose physicochemistry properties change with time. And there are other problems, such as weight, cost, and biocompatibility. Fortunately, artificial dielectric metamaterials with an appropriate structural design can exhibit similar properties to natural dielectric materials in the operating frequency band while being easily adjusted, and thus can be leveraged as an alternative to natural dielectric materials in some on-demand application scenarios.

Recently, metamaterials with parallel-plate capacitors formed by etched metal patches have been proposed to provide an alternative for DPs.[83,84] Their effective high permittivity and resultant homogeneity improvement have been demonstrated both in simulations and imaging experiments. In addition, the performance of these pads is on par with DPs. By positioning the metamaterial pad near the original local minimum of the transmitted field, the dark void can be effectively removed due to the improved field distribution. Evidently, these lightweight, compact, and readily available artificial high-permittivity metamaterials may be further popularized and adopted in clinical MRI.

3.2 Metamaterials with Novel Dispersion Relations

Dispersion relation is a basic feature that governs the propagation characteristics of electromagnetic waves within specific materials. Recently, metamaterials have been demonstrated to exhibit unusual dispersion relations, thus being capable of manipulating the propagation path of electromagnetic waves in unprecedented ways and leading to exotic electromagnetic phenomena. By virtue of these, many metamaterials with novel dispersion relations are proven to improve MRI by different mechanisms, including enhancing the field strength, guiding the RF flux, and tailoring the field profile, to name a few.

3.2.1 Magneto-inductive metamaterials

In addition to special TEM waves, metamaterials consisting of periodical elements have been verified to support another type of wave.[85] As shown in Fig. 4(a), an element driven by a time-varying current will couple with its neighbor elements via the

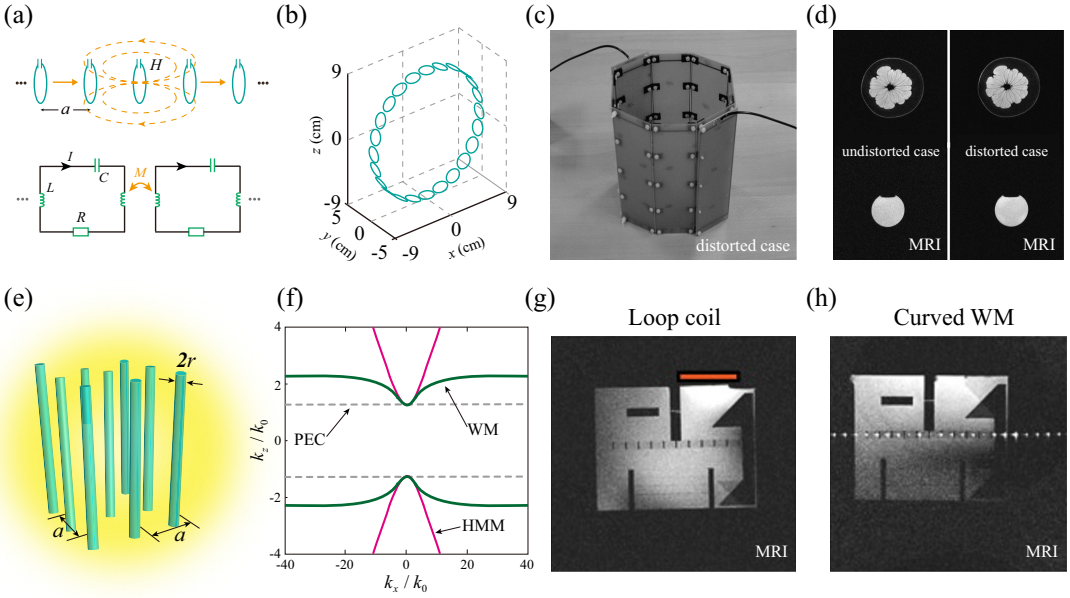

Fig. 4 MIMs and WMMs for MRI. (a) Sketch of a 1D MI waveguide consisting of coaxial capacitively loaded loops. (b) Equivalent circuit for the structure. (c) Photograph of a distorted flexible octagonal MI ring detector. (d) 1.5-T MRI experiment images of a pomelo fruit (upper images) and water-filled bottle (lower images) obtained from an undistorted and distorted MI ring detector. (e) Schematic diagram of WMM containing a dense array of metal wires. (f) Dispersions of a WMM formed from silver nanorods in three cases: with the PEC approximation (gray dashed lines), with spatial dispersion (thick green lines), and without spatial dispersion (thin magenta lines). 3-T MRI images of different phantoms obtained with a loop receiver coil and transferred (g) without the WMM or (h) with a 63 deg curved WMM. The position of the loop coil is indicated by an orange rectangle. The figures are reproduced with permission from (b) Ref. 86 © 2006 AIP, (c) and (d) Ref. 87 © 2010 Elsevier, (e) and (f) Ref. 88 © 2012 Wiley-VCH, and (g) and (h) Ref. 89 © 2009 Elsevier.

magnetic flux, which can induce a further current. The propagation of such a wave is generated by the recurrent relationship between the currents induced by magnetic coupling; it is thus termed a magneto-inductive (MI) wave. We take a simple one-dimensional (1D) array of unit cells featuring capacitively loaded loops as an example, in which only the nearest-neighbor coupling is considered and the loops are the same. In the equivalent-circuit model shown in the lower panel of Fig. 4(a), for the n'th loop, Kirchhoff's law gives

$$(j\omega L + j\omega C + R)I_n + j\omega M(I_{n-1} + I_{n+1}) = V_n, \tag{5}$$

where M denotes the mutual inductance, and I_n and V_n are the current and voltage of the n'th loop, respectively.

Assuming a traveling-wave solution of the form $I_n = I_0 \exp(-jnka)$, where k is the propagation constant and a is the period length, the dispersion relation of the MI waves can be derived,[85]

$$1 - \omega_0^2/\omega^2 - j/Q + \kappa \cos(ka) = 0. \tag{6}$$

Here, $\omega_0 = 1/\sqrt{LC}$ is the resonant frequency of the loops, $Q = \omega_0 L/R$ is the quality factor, and $\kappa = 2M/L$ is the coupling coefficient. If higher-order couplings cannot be neglected, the equation should instead be summed over all the coupling terms. The dispersion relation demonstrates that the propagation of MI waves is allowed within a certain frequency range, with an attenuation correlating to the Q-factor and the coupling. Furthermore, adjusting the coupling strength can affect the range of the passband, while changing its sign will determine the direction of wave propagation (forward or backward). For MRI applications, the equation is usually solved in a low-loss case so that the imaginary parts in the last two terms are approximated to be vanished. This assumption requires a high Q-factor and high coupling coefficient.

In practice, the formalism of an MI wave can be applied to other kinds of magnetic-coupled resonant RLC elements. For example, the aforementioned Swiss-roll array can support the MI waves under RF excitation.[90] However, an accurate description requires consideration of all coupling terms because the magnetic field produced by each roll decays slowly along the axis. MI waveguides, which have the capacity to form different devices using simple geometrical arrangements, have numerous potential applications in signal processing and energy guiding,[85,91] such as in delay lines, phase shifters, subwavelength lenses, power dividers, selective amplifiers, and of course, MRI.

Coil arrays have long been involved in the reception process of MRI, but the interactions between coils often need to be eliminated by overlapping or additional elements. As a potential alternative, a detector based on MI waves can take full advantage of the coupling between coils and achieve different functions with the aid of a specific current distribution.[86] Figure 4(b) presents a typical geometry for a rotational resonance ring detector, comprising $N = 24$ identical capacitively loaded loops. The MI wave will experience rotational resonance if the circumference of the circle is an integer multiple of the wavelength. Assuming a rotational magnetic dipole at the center of the detector as a source, which is analogous to a nucleus under MRI conditions, the current and power of each unit can be obtained by solving the matrix equation $V = ZI$. It has been demonstrated that the power extracted from a single loop can reach N times that of an uncoupled loop if extra optimized impedance matching is introduced between the former and the latter. Amplification of weak signals may be realized within the detector. As previously noted, the signals acquired by MRI contain many small-volume voxels, and the employment of this device thus requires further modification, since it only applies to signal gain in areas with fewer voxels. Instead, magnetic resonance spectroscopy (MRS), usually based on single-voxel and weak-signal measurements, offers a better platform for the MI detector.[86]

Another type of ring detector aims to maintain the nearest-neighbor coupling when the geometry is changed, thus avoiding detuning and frequency splitting.[87] The experimental setup for a distorted case is shown in Fig. 4(c). Here, the polygonal ring consists of several magnetically coupled rectangular LC resonators. Each of these is connected by a hinge to allow relative rotation, and additional structures are assembled to form nodes that essentially compensate for coupling variations. The most striking feature of this detector lies in the spatial distribution of its current, which is similar to that of a birdcage coil, but there are no rigid connections between adjacent elements. The results of imaging experiments [see Fig. 4(d)] speak volumes for the ability of MI ring detectors to provide good imaging quality under different shape configurations; that is, they can serve as flexible coils.

3.2.2 Wire-medium metamaterials

Wire-medium metamaterials (WMMs) represent a class of artificial electromagnetic structures composed of aligned metal wires (sometimes embedded into a dielectric substrate), as shown in Fig. 4(e). The contrast between the length and the diameter of the wires, as well as the contrast between the electromagnetic parameters of the metallic constituents and the dielectric matrix, results in extreme optical anisotropy and strong spatial dispersion,[88] respectively, and these are the direct causes of numerous novel properties.[45,92,93] WMMs were the first materials to realize negative permittivity.[88] For a set of metal wires aligned along the x axis, the permittivity tensor reads as

$$\bar{\bar{\varepsilon}} = \begin{pmatrix} \varepsilon_{xx} & 0 & 0 \\ 0 & \varepsilon_\perp & 0 \\ 0 & 0 & \varepsilon_\perp \end{pmatrix} \quad \text{and} \quad \varepsilon_{xx} = \varepsilon_0\left(1 - \frac{\omega_p^2}{\omega^2}\right). \tag{7}$$

Clearly, below the plasma frequency ω_p, the real part of ε_{xx} is negative. An isotropic negative-permittivity material requires the use of a 3D metal-wire array, while wires arranged along a single direction will lead to a hyperbolic dispersion relation if the axial and tangential permittivity components have opposite signs.[94]

It is found that the uniaxial dielectric tensor cannot rigorously describe a WMM, as it will exhibit strong spatial dispersion even in the large-wavelength limit. With the consideration of spatial dispersion, the nonlocal axial component is given as[88]

$$\varepsilon_{xx}(\omega, k_x) = \varepsilon_\perp\left(1 - \frac{k_p^2}{k^2 - k_x^2}\right). \tag{8}$$

Under the spatial-dispersion effect, WMMs are similar to uniaxial materials with extreme optical anisotropy; specifically, $\varepsilon_{xx} \to \infty$ in the dielectric tensor, and the metal wires are now

actually treated as perfect electric conductors (PECs). The dispersion of a sliver-nanorod WMM under three cases is shown in Fig. 4(f). The practical dispersion situation is generally somewhere between the two extreme assumptions (totally neglecting spatial dispersion and using the PEC approximation).

A salient feature of this spatial dispersion is the flat isofrequency contour (IFC), which supports a special kind of propagation mode: the so-called transmission-line (TL) mode.[95] The fundamental reason for this is that a series of parallel metal wires will behave as a coupled TL system. The TL modes have TEM polarization, and they travel along the wires with the same longitudinal wave vector and arbitrary transverse wave vector due to the peculiar IFC. The thickness of the wires is often chosen as a multiple of half the wavelength to satisfy the Fabry–Perot condition, thus ensuring efficient transmission,[96] while the fixed phase velocity enabled by TL modes permits the Fabry–Perot condition to apply to any angle of incidence, including a complex one.[97] In other words, electromagnetic waves, including their evanescent components, can be canalized from one side of the WMM to the other without disturbance. The canalization supported by WMMs is promising for application in subwavelength imaging, and this has been experimentally verified.[97] Intriguingly, a WMM can be regarded as a transverse magnetic (TM) counterpart of the Swiss roll.[98] To be more precise, Swiss rolls behave as "magnetic wires" near the resonant frequency and are narrowband and lossy, while WMMs are natural electric wires and are thus wideband and lossless.[97] Both can transfer spatial harmonics with specific polarization and both possess a pixel-to-pixel manner of imaging transmission. These unique characteristics can also be used to improve MRI.

An endoscope device for MRI exploiting the canalization of the TM field component within a WMM has been developed.[89] WMMs with different configurations were examined separately in an MRI machine to measure the effect of transferring an image within the endoscope, and the signal was collected by a loop coil at the end of the device. In addition to the straight shape, it was found that other strongly perturbed wire media—including convergent, divergent, and curved media—could always achieve effective collimation. Furthermore, it was found that the convergent and divergent WMMs could concentrate and extend the image, respectively, providing more possibilities for MRI. For example, a focused magnetic field could be imaged with more powerful surface coils. With the curved WMM, the image was not deformed, even with a total bending angle of 63 deg, as shown in Figs. 4(g) and 4(h). Although the introduction of the endoscope does not achieve obvious enhancement of the SNR, it provides the ability to transfer the information-carrying RF magnetic field to places where the static magnetic field is relatively small, thus allowing for the use of magnetic devices, which would otherwise be impossible. In addition, assuming that more flexible and harmless media are deployed and no impedance problems occur, the assembled endoscope may be harnessed for *in vivo* MRI.

Subsequently, an optimized WMM endoscope with a length of 2.5 m, which is almost half the wavelength of 1.5-T MR, was tested in an MRI system.[99] The evanescent waves were transformed into propagating TEM waves in the WMM, and this was accompanied by high efficiency because Fabry–Perot resonance occurs. The polarization selectivity can be further eliminated by oblique WMMs, enabling full reconstruction of the near field.[100] It has also been found that better imaging quality requires detection of signals at the center due to the excitation of standing waves;[99] this is manifested in the internal electromagnetic field distribution of the endoscope and in the experimental results. In this way, an enhanced SNR, which was not achieved by the above-described endoscope prototype, can be realized. However, the large volume of the WMM device is a challenge, one that restricts potential applications unless it is appropriately tackled.

Finally, a set of well-designed metallic wires has been demonstrated to strongly enhance or suppress the magnetic field in ultrahigh-field MRI by satisfying the Kerker scattering conditions;[101] this subtly leverages the constructive or destructive interference of scattered fields.

3.2.3 Composed right-/left-handed transmission-line metamaterials

The above-described metallic resonant structures, including Swiss rolls and SRRs, are familiar configurations for constructing left-handed materials, but they are limited by losses and discontinuities. The development of the composed right-/left-handed transmission line (CRLH-TL) provided a good solution to these problems and has promoted the design of microwave circuits and innovations in microwave devices.[102] A schematic of such a TL is shown in Fig. 5(a), in which the electric and magnetic field distributions are marked by black solid and red dashed lines, respectively. A TL model of circuit-based metamaterials and the corresponding lossless equivalent circuit of a CRLH-TL are shown in Figs. 5(b) and 5(c), respectively. It is of note that although one can just add series capacitors and parallel inductors to obtain pure left-handed characteristics, the right-handed part is unavoidable in practical circuits; hence, CRLH is the general case.

The dispersion relation of the CRLH-TL can be obtained by virtue of TL theory. It exhibits left-handed properties at high frequencies and right-handed properties at low frequencies. There is a stopband between the left- and right-handed passbands, which can be eliminated by changing the lumped parameters to match the series frequency (ω_{se}) and shunt frequency (ω_{sh}), meaning the CRLH-TL is "balanced." Due to the similarity between the telegraph equations and Maxwell's equations, a CRLH-TL can be described by effective parameters,

$$\varepsilon = \varepsilon(\omega) = C_R - \frac{1}{\omega^2 L_L} \quad \text{and} \quad \mu = \mu(\omega) = L_R - \frac{1}{\omega^2 C_L}. \tag{9}$$

Accordingly, it is not difficult to create CRLH-TLs with diverse and tunable responses. With proper design and loaded lumped elements, CRLH-TL metamaterials can be fabricated into many devices, including couplers,[105] antennas,[106,107] and topological insulators,[108,109] and can also be exploited in MRI. In terms of a conventional right-handed TL, resonance occurs when the following condition is satisfied:

$$\theta = \beta l = \left(\frac{2\pi}{\lambda}\right)\left(\frac{m\lambda}{2}\right) = m\pi, \quad m = 1, 2, 3, \ldots, \tag{10}$$

where θ is the electrical length, β is the propagation constant, l is the period length, λ is the wavelength, and m is the resonance order. In a CRLH-TL, m can also be a negative integer or zero. Zero-order resonance (ZOR) can be observed in a balanced

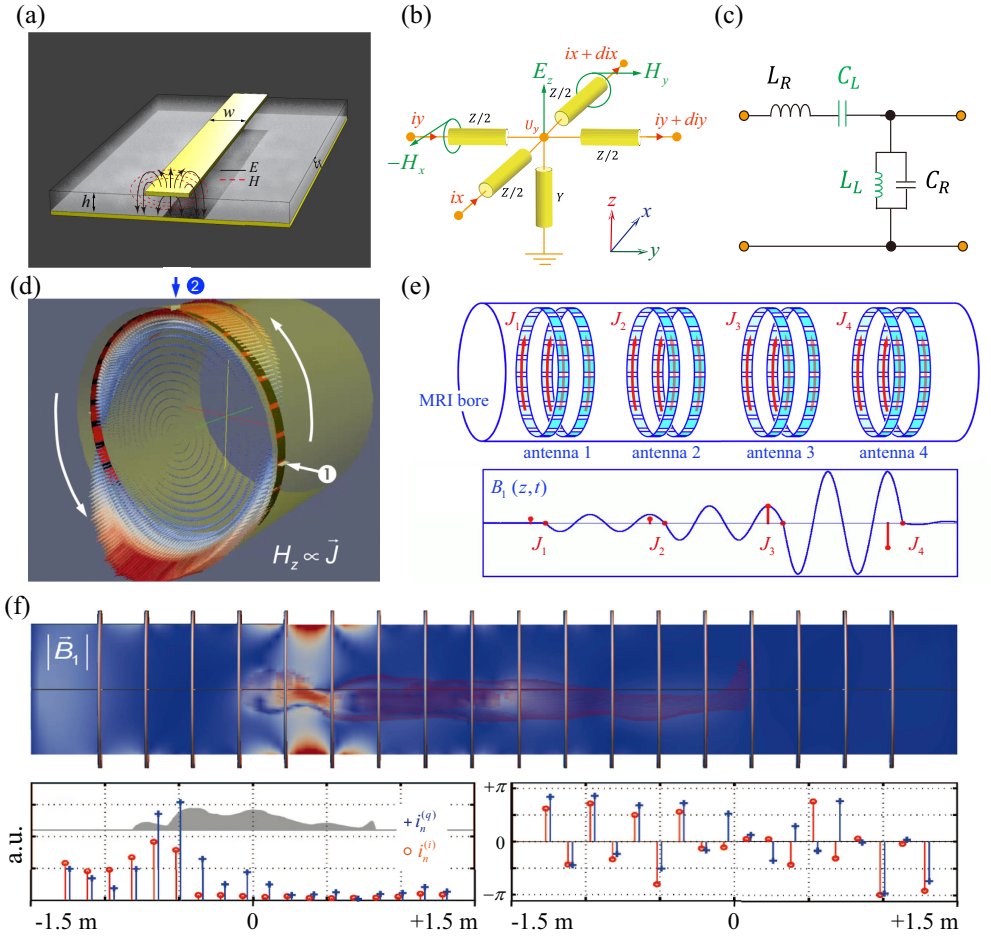

Fig. 5 CRLH-TL metamaterials for MRI. (a) Schematic of a TL, in which the electric and magnetic field distributions are marked by the black solid and red dashed lines, respectively. (b) TL model of a circuit-based metamaterial. (c) The corresponding equivalent-circuit model of the 1D TL structure. (d) Simulated model and magnetic field distribution of a CRLH ring antenna with the current flowing along the surface at resonance. (e) Schematic diagram of the adaptivity of a CRLH ring antenna system realized by tailored current distribution: unidirectional transmission (antenna 1), coherent amplification (antennas 2 and 3), and active attenuation (antenna 4). The frequency is exaggerated for visibility. (f) CRLH ring antenna system with on-demand magnetic field distribution (top panel) for a larynx imaging case. The amplitudes and phases of the in-phase and quadrature current excitations of each unit cell are shown in the bottom panels. The figures are reproduced with permission from (d) and (e) Ref. 103 © 2011 IEEE, and (f) Ref. 104 © 2013 IEEE.

CRLH-TL with a singular nonvanishing transition frequency at $\beta = 0$, and the corresponding guided wavelength tends to infinity.

The frequency of the ZOR depends only on the lumped parameters (which decide the value of the matched frequency) and is not limited by physical size. This feature is extraordinarily useful in antenna miniaturization, and it may solve the problems associated with fabricating dedicated small resonators. More interestingly, a CRLH-TL can yield a rather uniform current/voltage distribution when the terminals are short/open, and the former is suitable for generating a homogeneous magnetic field.[110] Furthermore, in the context of ultrahigh-field MRI ($\geq$7 T), the shorter wavelength becomes comparable to the size of the sample or element, incurring more wave behaviors that will inevitably distort the homogeneous distribution of the RF magnetic field.[111] One possible solution to this problem is to replace the traditional RF transmitter coil with a CRLH-ZOR coil element to preserve the uniformity of the transmitted magnetic field.[110] Considering the size-free nature of the ZOR, this coil element theoretically can be made into arbitrary lengths to accommodate imaging at different body parts. It can also form multichannel coil arrays[112] or be employed at other field strengths by altering the lumped parameters.

Another instructive tool for ultrahigh-field MRI takes advantage of traveling waves. In principle, the spatial variation of the standing-wave amplitude can be transformed into the phase variation of a traveling wave,[113] and this may result in a more uniform RF magnetic field and allow a larger ROI at the cost of decreased efficiency and sensitivity. The most appealing aspect of this approach is that the receiver does not need to be close to the sample: it can be anywhere along the bore as long as it is coupled to the waveguide propagation modes. Nonetheless, a

closed-end antenna system at the end of the MRI bore is often exploited to transmit traveling waves; hence, the available space and thus the patient's comfort are greatly reduced, which restricts clinical applications.[103]

Inspired by the CRLH-TL, a CRLH ring antenna system has been developed to manipulate the RF magnetic field distribution in ultrahigh-field MRI. This system contains building blocks similar to the unit cell of the ZOR coil, but they are bent to form a ring.[103] Due to the constraints imposed by the continuity of fields at nodes on the periodical boundary conditions, it has different properties from a planar structure; that is, it supports a full-wave resonance mode along its circumference. With proper design and optimization, the current distribution in a ring antenna may closely mimic the surface currents of the TE_{11} mode [see Fig. 5(d)]; hence, a system arranged with several ring antennas can naturally serve as an RF coil for traveling-wave MRI. In addition, the circular shape is inherently adapted to the MRI bore, avoiding any impact on the original space and leaving a large accessible volume.

Imaging experiments have provided a proof of concept for this system in extended-region and high-resolution imaging.[114] Such a system may also perform diverse functions if the amplitude and phase of the currents in individual ring antennas are tailored. Figure 5(e) presents the realized features, including unidirectional transmission, coherent amplification, and active attenuation. Flexibly tailoring the distribution of the RF magnetic field along the axis is no longer a purely theoretical idea, though it may not be achieved very easily. Furthermore, with the help of algorithms and databases, the system has the potential to solve inverse problems based on the characteristics of the imaging area, thus rapidly adjusting each element in real time to achieve a target magnetic field distribution,[104] as shown in Fig. 5(f).

4 Metamaterial Resonators for MRI

The capacity for metamaterials to improve MRI has been fully demonstrated by a variety of devices. However, these applications are often restricted by factors including volume limitations, signal loss, and limited enhancement. In Sec. 3, MRI-enhancing traditional metamaterials that exhibit tailored extreme effective electromagnetic parameters or exotic dispersion relations, together with their impacts on the propagation of electromagnetic waves during the MRI process, are reviewed. Recently, another subtype of metamaterial, termed as metamaterial resonator (MMR), has attracted wide interest due to the improved efficiency and increased practicality of implementation for their use in MRI. Instead of being defined by effective parameters or dispersions as traditional metamaterials, MMRs are featured by their resonance-induced field-redistribution property, therefore enabling them to sculpt the electromagnetic field distribution due to peculiar field patterns of different resonant modes. These resonators may be applied as wireless coils to combine with the body coil or be deployed as passive enhancement devices compatible with other receiver coils. The SNR enhancement ratios of several typical MMRs are plotted in Fig. 6; it can be seen that they reach unprecedented levels. Note that these values are only for reference due to the distinctive experimental conditions in which they were obtained, such as the size of the resonators, ROI areas, imaged samples, field strengths, and sequences. Some works have not been included here due to their lack of SNR measurement or experimental validation. In addition, a large number of works employ the results of MRI obtained with the birdcage coil in transceiver mode as an reference, which is, however, not a routine way for practical operation. Instead, combining the birdcage transmitter coil and local receiver coil can realize much better performance. Therefore, we must point out that this trick may overstate the impact of some MMR designs in clinical MRI to some degree, which should be evaluated on a case-by-case basis. Anyway, we anticipate that with further research, more reasonable designs, performance optimizations, and innovative mechanisms are being introduced, making MMRs a fascinating and fertile soil for the application of metamaterials to improve MRI.

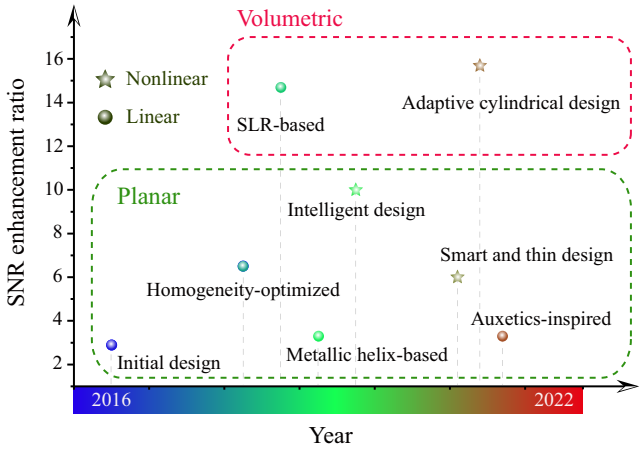

Fig. 6 SNR enhancement ratios of typical MMRs. Different types are distinguished by symbols and colors. For planar MMRs, the ratio is measured 2 cm above the surface; for volumetric MMRs, the ratio is measured in the ROI.

4.1 General MMRs

Most often, the electromagnetic responses of metamaterials can be predicted by effective parameters or described by multipole expansion.[115] However, eigenmode (or modal) analysis is better suited to the scenario of near-field confinement and manipulation because it intuitively reveals spatial electromagnetic field profiles. This analysis can be conducted with the aid of analytic methods or numerical simulations.

The first MMR proposed for improving MRI consisted of several metallic wires periodically arranged as a 14×2 array,[59] as shown in Fig. 7(a). To get access to lower resonance frequencies (or smaller metamaterial sizes), the resonator was immersed in distilled water with a high permittivity of about 81. In this situation, multiple eigenmodes are generated due to the giant coupling between adjacent wires,[45] which can be adjusted by the period lengths. When an incident magnetic field is applied, different eigenmodes can be excited corresponding to different frequencies and electromagnetic field amplitude distributions. Among these, the fundamental mode is most frequently chosen because it has the greatest penetration depth. Distinctive current distributions along the wires contribute to different magnetic field patterns for these eigenstates. One commonality between them is the localized magnetic field at the center and localized electric field at the edges, which is analogous to Fabry–Perot resonance.

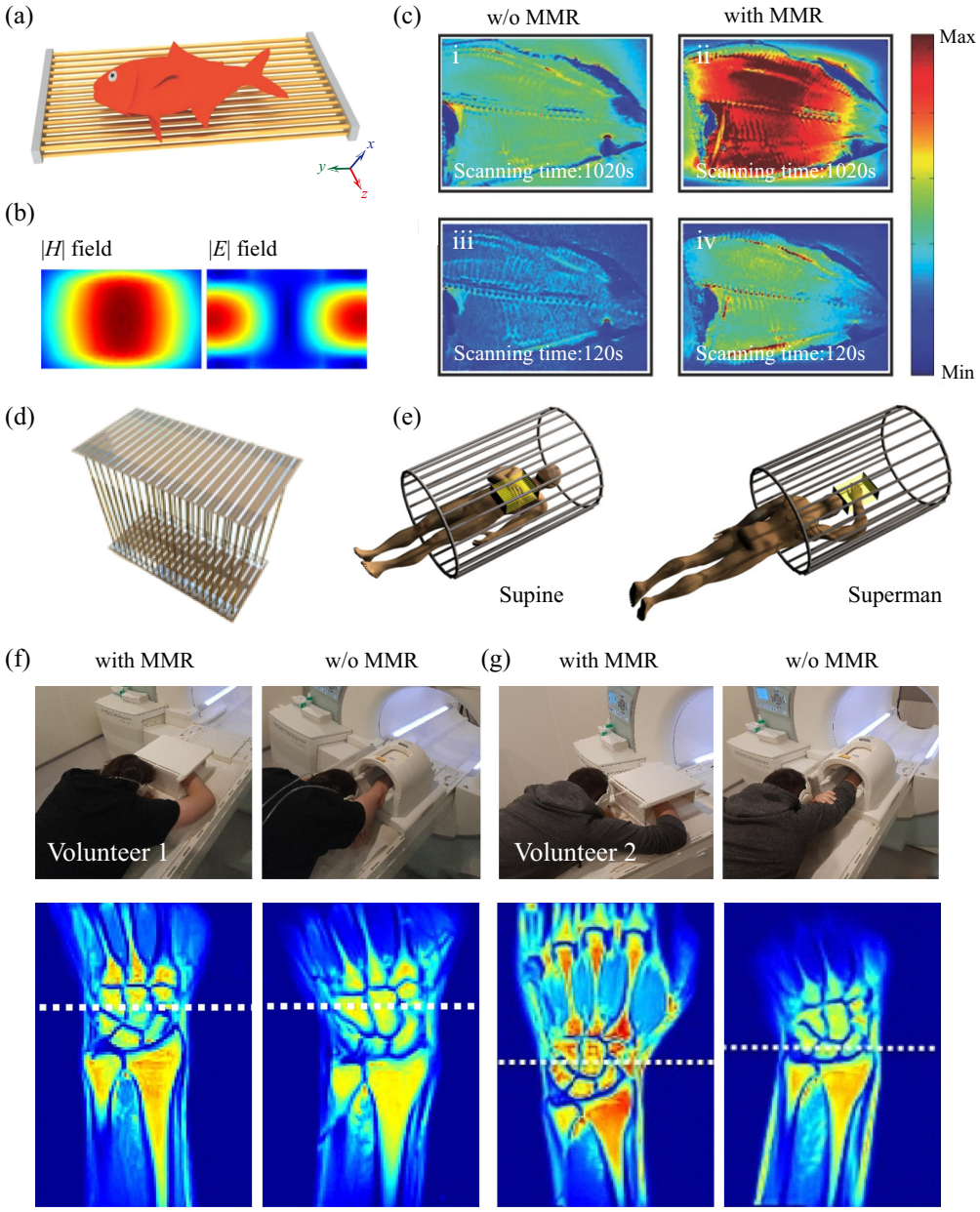

Fig. 7 General MMRs for MRI. (a) Schematic view of a planar MMR composed of metallic wires. (b) The electromagnetic field distribution above this MMR for the fundamental mode. (c) 1.5-T *ex vivo* MRI images of fish with scanning times of 1020 s [(i) and (ii)] or 120 s [(iii) and (iv)] in the absence of the MMR [(i) and (iii)] or in the presence of the MMR [(ii) and (iv)]. (d) Sketch of the design of a volumetric MMR. (e) Illustration of possible clinical scenarios for deploying volumetric MMRs: supine position (left panel) and superman position (right panel). (f) and (g) Experimental setups and SNR maps of 1.5-T wrist MRI of two volunteers in the superman position with different settings: whole-body birdcage coil in transceiver mode in the presence of volumetric MMR (the first and third columns); extremity coil in transceiver mode (the second and fourth columns). The figures are reproduced with permission from (a) and (c) Ref. 59 © 2016 Wiley-VCH; (b) Ref. 116 © 2018 Elsevier, licensed under a CC-BY 4.0 International License; (d) and (e) Ref. 37 © 2018 Wiley-VCH; and (f) and (g) Ref. 117 © 2022 Elsevier.

These drastically enhanced magnetic field patterns are applied in MRI by precisely tuning the frequency between a specific eigenmode and the Larmor precess, as shown in Fig. 7(b). Notably, the orientation of the MMR is not arbitrary, and to guarantee that an eigenmode is correctly excited, the magnetic field components should be perpendicular to the surface. Figure 7(c) shows MRI *ex vivo* images of fish obtained by a set of comparative experiments performed in a 1.5-T system. It can be concluded that the MMRs can effectively increase the MRI imaging quality and produce higher resolutions

[(i) versus (ii) and (iii) versus (iv)] or enable reduction of the scanning time and enhancement of safety without decreasing the SNR [(i) versus (iv)]. Both the transmitted and received RF fields will undergo an increase in the vicinity of the structure, and the effect rapidly decays with distance. In other words, suitable placement of the sample near the introduced MMRs yields a boost in the transmitting efficiency and receiving sensitivity of MRI. Subsequent human *in vivo* imaging experiments[116] have further confirmed the ability of MMRs to locally enhance the RF magnetic field and thus the imaging quality near the ROI.

When it comes to clinical applications, distilled water may not be a practical choice; thus, more compact and flexible structures are highly desirable. One feasible method to satisfy the need for miniaturization is to introduce extra capacitance.[118] The use of other high-permittivity media (for example, an aqueous suspension of calcium titanate in water) can also circumvent the need for a large and rigid structure.[35] Most importantly, the flexibility of MMRs opens up new possibilities for constructing dedicated shapes to conformally fit the anatomy of patients and/or for integration with other well-established techniques.

The magnetic field enhancement effect of MMRs is largely dependent on the spectral matching between eigenmodes and Larmor precession. Therefore, hybrid multiband MMRs may simultaneously have a marked impact on different types of NMR. For instance, dual-nuclei MRI can provide more biochemical information than routine proton imaging, but the nonproton part often has a limited SNR owing to low concentrations. A combination of different configurations of MMRs may appropriately solve this issue.[36,119] In the quasi-static approximation, magnetic dipoles (or electric dipoles) can be equivalently mimicked by short (or long) wires. In one work, two sets of zigzag-shaped metallic strips were alternately assembled to yield a dual-band response[36] tuned for MR of ^{1}H and ^{31}P. Harnessing different orders of eigenmode for the two nuclei is beneficial for minimizing the interactions between different resonators (for example, the first/third mode of a short/long wire resonator). These novel designs can be easily extended to other dual-nuclei MRI applications, and they serve as a motivation for future examinations of multinuclear MRI.

The above MMRs are mostly based on unit cells featuring metallic wires. Recently, some other building blocks have been reported for fabricating MMRs with 2D periodicity,[120,121] which may impose fewer limitations on the placement orientation. In addition to planar geometry, volumetric MMRs dedicated to particular body parts (e.g., wrist, breast, and extremities) have been suggested to compensate for the possible low SNR caused by the distance between the coils and the ROI.[37,117,122] The prototype shown in Fig. 7(d) represents a typical volumetric design based on a periodic array of coupled split-loop resonators (SLRs). This configuration is similar to the so-called metasolenoid,[123] and it can also be regarded as an extended version of a planar metallic wire array. The overlapping strips on opposite sides of the top and bottom PCBs allow the frequency to be tuned. The coupled SLRs operate as a waveguide in the y direction, and multiple reflections from the ends form standing-wave patterns for the eigenmodes.[37] Evidently, a more homogeneous magnetic field is in accord with the requirements of the original transmitted RF field. Two major working scenarios are depicted in Fig. 7(e): the "supine" and "superman" positions. Both positions can assure that the B_1^+ components are perpendicular to the SLRs, and the fundamental eigenmode can thus be used.

Such volumetric MMRs can be considered as a kind of wireless coil for MRI because the way in which they work is partially the same; that is, a wireless coil is put around an ROI to pick up the relaxation signal and enable a high sensitivity compared to a birdcage coil in transceiver mode, and the transmitted magnetic field is generated by a body coil or otherwise. Nonetheless, a completely wireless coil should incorporate functions including wireless signal conditioning, wireless data transmission, wireless control, and wireless power supply to avoid the need for cable connections.[124] As a consequence, it may be more accurate to describe the proposed volumetric MMRs as cableless local (or surface) coils. The feasibility of volumetric MMRs has been numerically and experimentally demonstrated in recent studies.[117,122] Figure 7(f) presents simulated B_1^+ and SNR maps inside a birdcage coil with and without the proposed volumetric resonator of volunteer 1. Marked localization of the magnetic field contributes to a drastic enhancement of the transmitted RF field, together with a moderate increase in SNR. To maintain safety, one may reduce the applied power by a factor of 33 without decreasing B_1^+. Figure 7(g) presents the experimental setup and SNR maps of the wrists of volunteer 2 in a superman position. The volumetric MMR coupled to the birdcage coil has significantly improved transmitting efficiency and provides better sensitivity in the reception process. The results in both the coronal and transverse planes demonstrate that the volumetric MMR can provide comparable results to an extremity birdcage coil, which has been widely used in clinical MRI. Recently, it has been suggested that the topologically protected edge states of a 1D Su–Schrieffer–Heeger chain can be reproduced in a coupled SLR array, further sculpting the magnetic near field of volumetric MMR in specific ways.[125]

4.2 Tunable MMRs

It is noteworthy that the locally redistributed magnetic field generated by previous designs is inhomogeneous over the volume of MMRs. Furthermore, fine-tuning their spectral matching is difficult. Therefore, novel designs with better uniformity and/or tunability are highly desirable. Some research has been carried out that attempts to tackle these issues.[38,126–129]

Figure 8(a) shows an optimized MMR in which high-permittivity water blocks are only placed at the edges. The high contrast of permittivity between the middle and the edges can reshape the magnetic field pattern into a uniform distribution.[126] In addition, the effective permittivity of the background medium can be further altered by changing the volume fractions of different dielectric inclusions and the filling factor of the water blocks. However, the magnetic field amplitudes still have a cosine-like profile across the metallic wires.

In one study considering an MMR with structural capacitances, the overlapping patches were fabricated to be movable, and the surrounding plates had a specific wedge shape to provide a nonuniform capacitance distribution,[127] as shown in Fig. 8(b). As such, an enlarged area of a homogeneous magnetic field, which is desirable in practical use, can be realized via fine control. Local modification of certain unit cells is also a straightforward approach to tune volumetric MMRs.[129] By rewriting the coupled mode theory (CMT) equation for this system, one can achieve an arbitrary target magnetic field by tuning the intrinsic losses of each unit cell.[128] The tuning procedure is dependent on the pumping of the microfluidic layer in this structure. Although

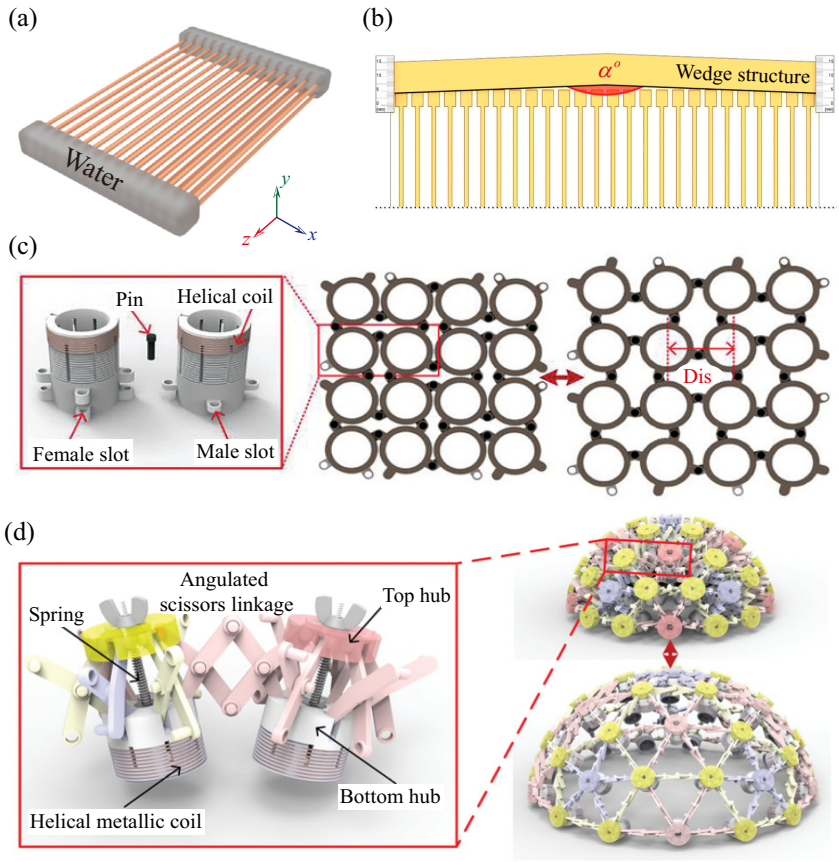

Fig. 8 Tunable MMRs for MRI. (a) Sketch of an MMR with tunable water filling factor. (b) Configuration of an MMR with movable metallic patches and an on-demand adjustable wedge shape. (c) Illustrations of structural deformation between adjacent unit cells and of a complete 2D auxetic MMR. (d) Similar to (c), but for the 3D case. The figures are reproduced with permission from (a) Ref. 126 © 2018 American Physical Society, (b) Ref. 127 © 2019 AIP, and (c) and (d) Ref. 38 © 2021 Wiley-VCH.

the method is not very practical, it offers a paradigm that fundamentally treats the field-reforming process as an inverse problem.

The final example of this type is a combination of MMR and auxetics,[38] which refers to materials with a negative Poisson's ratio. Figures 8(c) and 8(d) show the basic layout and deformation of 2D and 3D tunable structures for such devices, respectively. A classical rotating polygonal model is adopted for the 2D metallic helix arrays to obtain auxeticity. As a consequence, the horizontal and vertical distances between adjacent building blocks can be simultaneously contracted or expanded. For the 3D prototype, another model, referred to as a Hoberman sphere, was developed, which completed the expected deformation by a scissor-like action of joints. This deformation leads to tuning of the frequency and consequent modification of the field. By virtue of the inherent scalability and adaptability of auxetic structures, they can be employed for imaging different body parts in a conformal fashion.

Overall, the tunable MMRs described in this section, through their different mechanisms, either introduce feasible means for optimization of the field distribution or provide extra degrees of freedom to realize the fine-tuning of the frequency, thereby improving the prospects for clinical MRI applications to some degree.

4.3 Nonlinear MMRs

As described above, the spatial field inhomogeneities generated by MMRs have been widely investigated; however, the very different impacts of inhomogeneities on the transmission and reception processes are much less well understood. Specifically, frequency-dependent MMRs will enhance the magnetic field during the transmitting and receiving phases simultaneously. However, unlike inhomogeneities in the receiving phase, which can be corrected in postprocessing, inhomogeneities during the transmitting phase cannot be corrected and will result in problems. From the imaging perspective, enhancement of the transmitted field will lead to deviations of the FA from the original settings, thus leading to artifacts. A commonly adopted solution has been to calibrate the RF power,[37,38,59,118,120,126,127,129,130] which can avoid overtipping and ensure that the actual FA is equal to the settled nominal FA. However, reducing the applied power results in the need for an extra process of manual adjustment or procedural calibration, and this may contribute to new troubles, such as a low FA at a distance, especially for planar MMR with distance-decay enhancement. Furthermore, a nonuniform transmitting field may pose a potential threat of tissue heating and high specific absorption rate values without additional modification of the FA.

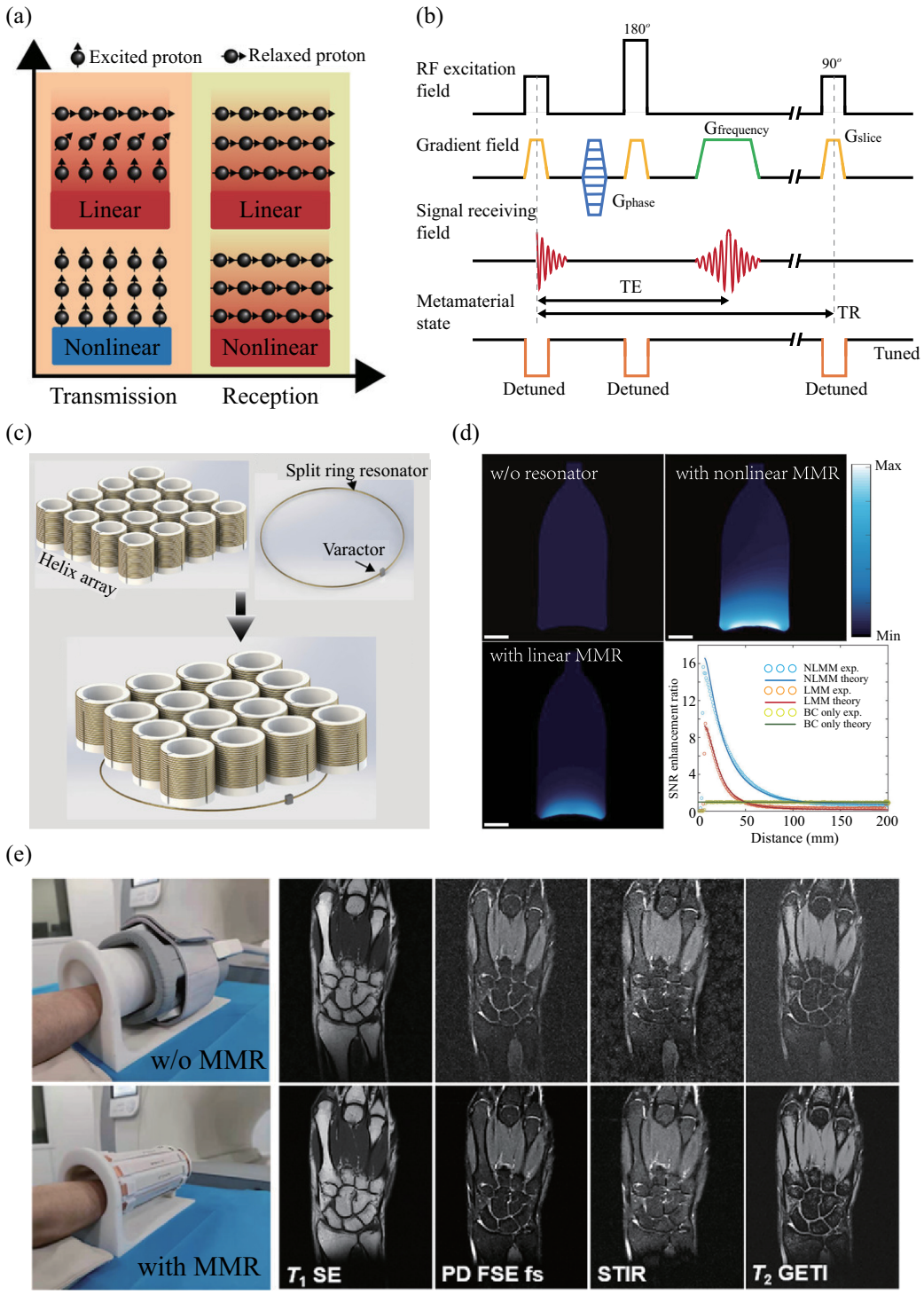

Fig. 9 Nonlinear MMRs for MRI. (a) Conceptual illustration of the working principle for linear and nonlinear MMRs. (b) Schematic diagram of MRI pulse sequence and response of nonlinear MMRs. (c) Sketch of the configuration of a nonlinear MMR consisting of a helix array and a varactor-SRR. (d) 3-T MRI images of a mineral-oil phantom captured for three cases: body coil only (top left), and body coil with a nonlinear (top right) and linear (bottom left) MMR. The relevant SNR enhancement ratio curves as functions of distance are also shown (bottom right). (e) Experimental setups and images of a 1.5-T wrist MRI using different sequences: with flexible coil (top panels); and with adaptative cylindrical nonlinear MMR (bottom panels). The figures are reproduced with permission from (a), (c), and (d) Ref. 40 © 2019 Wiley-VCH, and (e) Ref. 39 © 2021 Wiley-VCH.

Fortunately, nonlinearity has shown extensive potential in bio-imaging applications.[131] It also provides a way to yield dynamic responses during different MRI phases [see Fig. 9(a)]. The crucial factor is that the transmitted and received fields vary in RF power and chronological order,[39] and this is the foundation for introducing nonlinearity. Nonlinear responses can effectively enhance the sensitivity of reception while avoiding distortion of transmission. Figure 9(b) schematically shows the state of a nonlinear MMR within a pulse duration of the spin-echo sequence.

Nonlinearity has been previously applied in MRI using other techniques. For example, some dedicated receiver coils need to be detuned during transmission and vice versa, and this is realized by nonlinear elements. In one work, a varactor-loaded SRR was combined with a metallic helix array to construct an intelligent nonlinear MMR,[40] as shown in Fig. 9(c). The varactor exhibits a voltage-dependent capacitance, allowing for nearly uniform excitation and markedly increased reception. The oscillation amplitude of the varactor is highly dependent on the external field strength; the response of the nonlinear MMR behaves similarly and can be further modified by the coupling strength and frequency detuning between the helix array and varactor, according to the CMT. Figure 9(d) shows that the SNR of an image obtained by the body coil without an MMR is homogeneous throughout the phantom. Both linear and nonlinear MMRs significantly enhance the local SNR, which decays rapidly with distance. It can also be seen that the nonlinear MMR produces a greater SNR enhancement; it can thus be inferred that the introduced varactor element and the avoidance of reduced RF power can result in an additional increase in the magnetic field. A similar design has also been suggested for developing a compact nonlinear MMR composed of a metallic wire array and a loaded SRR.[132]

Another example is an MMR based on a common metallic wire array, which was assembled with an additional digital switching system.[133] In this system, the inductor senses the applied RF magnetic field and induces an AC signal, which is then compared to a threshold voltage and digitized in a comparator. The generated digital signal is then downconverted to produce the desired duty cycle using a counter and timer, and it is further fed to diodes, which are each connected to control the response of an individual unit cell.[133] In this work, it was validated that the imaging effect was consistent with the aforementioned RF-sensitive nonlinear structure. Although the diode-switch matrix may introduce unnecessary losses, the switching system offers a universal nonlinear paradigm for various kinds of MMR.

The last instance is an adaptive cylindrical MMR, constructed from copper strips and conductive tapes on opposite sides of the dielectric substrate to create resonance, and the control system for the diodes selectively activates the response. This configuration partially resembles a birdcage coil containing two rings and several rungs. The surface current distribution along each strip is proportional to the sine of its azimuth. Consequently, the magnetic field is highly homogeneous in both the radial and axial directions. In addition, the cylindrical design ensures that the field can be enhanced regardless of the incident direction, which is of great benefit for circularly polarized B_1^+ fields. Both field homogeneity and polarization insensitivity were integrated into a nonlinear MMR for the first time using this design, and systematic experiments were conducted to evaluate its feasibility and effectiveness. Figure 9(e) shows the setup of a 1.5-T MRI system using the proposed structure and a flexible coil, along with images of a human wrist obtained from this system. With various clinical sequences, better images were always acquired in the presence of the MMR. This may pave the way for employing MMRs in practical clinical MRI.

5 Conclusion and Outlook

Metamaterials, with their abundant novel physical characteristics and unprecedented ability to tailor electromagnetic waves, have been widely applied to improve MRI. In this article, first, the principle of MRI is described, numerous metamaterials for use in MRI are then categorized in accordance with their mechanisms, and their applications are reviewed. Over recent decades, the use of metamaterials in MRI commenced with conceptual hypotheses, continued with proof-of-principle devices, and finally led to a series of innovative solutions. It has been demonstrated that metamaterials can play different roles in improving MRI, such as enhancing the imaging quality, reducing the scanning time, ameliorating the inhomogeneity of the magnetic field, decreasing the electromagnetic radiation to which a patient is exposed, and extending the imaging region, to name a few.

We emphasize that MRI is essentially a clinical method, and thus the design of metamaterials should focus on solving practical problems in this field (e.g., poor SNR in low-field MRI and inhomogeneity in high-field MRI). Despite the fact that a vast array of metamaterials has been reported to improve MRI from certain aspects, there are few designs being commercially employed in practical scenarios. For traditional metamaterials, the bulky structure and limited enhancing effect are likely to be the major limiting factors in preliminary applications. In contrast, MMRs possessing compact architecture and considerable enhancement factors seem more promising, and they indeed go further. Nonetheless, the spatial inhomogeneity and potential health risks introduced by MMRs still require innovative solutions to address before clinical promotion. In addition, the performance of MMRs for different imaging sequences and tested objects should be carefully evaluated and compared with commercial coils for reference, to assess whether the deployment of MMRs deserves the resultant extra modification. These above require combined efforts of professionals and researchers working in RF, medical health care, electromagnetic compatibility, material science, and so on.

In our opinion, a successful application of metamaterials in MRI requires the following considerations on a case-by-case basis:

(1) Enhancement: For devices designed to boost a certain metric (e.g., SNR), the extent of the increase should be not only sufficient to compensate for the loss or noise caused by the addition but also great enough to provide notable improvement.

(2) Feasibility: The compatibility between metamaterial devices and the MRI equipment should be comprehensively considered, including the space they occupy, their impact on the electromagnetic circumstances, and safety concerns, to name a few. Among these, safety should be particularly underlined; thus overall simulations and preclinical examinations must be performed to assess potential health risks before the practical application of these devices.

(3) Tunability: The devices require some adjustable range in frequency and response due to the inherent variability of imaging according to environmental factors and sample conditions.

(4) Homogeneity: The devices, whether employed to enhance the magnetic field or otherwise, should avoid disturbing the static field as much as possible; they should also maintain the original uniform distribution of the RF magnetic field (or the FA), which will avoid the need for additional complex processing.

It is clear that the improvement of MRI with metamaterials is a topic that has not yet been fully explored. MRI can serve as an appealing platform for introducing and exploring a variety of metamaterials, and this can in turn inject new vitality into MRI. We would like to give a few examples to offer some insights into these possibilities. (1) Zero-index metamaterials (ZIMs) can be placed near the origin of the electromagnetic parameter space and can have many exotic properties.[134,135] Most conspicuously, when propagating in a ZIM, electromagnetic waves will have a wavelength tending to infinity and a phase accumulation of zero. In addition to the aforementioned local modifications, MRI ZIMs have the potential to construct a magnetic field with a quasi-uniform amplitude and phase, which is rather appealing for improving the homogeneity of the RF magnetic field. (2) Recently, a class of highly anisotropic metamaterials with hyperbolic dispersion has come into view.[94,136] Among these, hyperbolic cavities[137–139] possessing high Q/V values, abundant resonant modes, and anomalous scaling laws may meet the needs of efficient, tunable, and miniaturized MRI devices. (3) With the development of computational science, the expectation of real-time dynamic adjustment of the unit cells of a metamaterial has become a reality. The overall responses of metamaterials can be actively controlled by electrical, optical, thermal, and other methods, leading to more modern intelligent metamaterials and metadevices.[140–142] The combination of metamaterials and coding, algorithms, and programming may further allow the accommodation of different samples, environments, and imaging requirements in MRI systems.

Some metamaterials initially designed for MRI can also be extended to other interdisciplinary realms, such as MRS, which is similarly based on NMR. Some research has suggested the practicability of using metamaterials in MRS to enhance component detection.[35,36,86] In addition, MMRs can be applied in wireless power transfer to generate a region with a relatively uniform magnetic field,[143,144] or for the visualization of eigenmode patterns with the aid of MRI systems.[12] The precise and powerful manipulation of electromagnetic fields by these metamaterials may allow more advantageous applications in communications, sensing, and other fields.

In the future, we anticipate more interesting interactions between metamaterials and MRI, and this will require new insights and persistent efforts by researchers. These works could lead to convincing proof of the crucial impact of metamaterials in MRI, and they could also provide promising approaches to addressing the pressing needs of MRI-related scientific research and clinical medicine.

Disclosures

The authors declare no conflicts of interest regarding this work.

Acknowledgments

This work was supported by the National Key R&D Program of China (Grant Nos. 2021YFA1400602 and 2023YFA1407600), the National Natural Science Foundation of China (Grant Nos. 91850206, 12374294, and 12004284), and the Chenguang Program of Shanghai (Grant No. 21CGA22).

References

1. E. M. Purcell, H. C. Torrey, and R. V. Pound, "Resonance absorption by nuclear magnetic moments in a solid," *Phys. Rev.* **69**(1–2), 37–38 (1946)
2. F. Bloch, "Nuclear induction," *Phys. Rev.* **70**(7–8), 460–474 (1946).
3. C. Boesch, "Nobel prizes for nuclear magnetic resonance: 2003 and historical perspectives," *J. Magn. Reson. Imaging* **20**(2), 177–179 (2004).
4. P. C. Lauterbur, "Image formation by induced local interactions: examples employing nuclear magnetic resonance," *Nature* **242**(5394), 190–191 (1973)
5. G. B. Frisoni et al., "The clinical use of structural MRI in Alzheimer disease," *Nat. Rev. Neurol.* **6**(2), 67–77 (2010).
6. V. O. Puntmann et al., "Outcomes of cardiovascular magnetic resonance imaging in patients recently recovered from coronavirus disease 2019 (COVID-19)," *JAMA Cardiol.* **5**(11), 1265–1273 (2020).
7. M. D. Fox and M. E. Raichle, "Spontaneous fluctuations in brain activity observed with functional magnetic resonance imaging," *Nat. Rev. Neurosci.* **8**(9), 700–711 (2007).
8. U. Dannlowski et al., "Limbic scars: long-term consequences of childhood maltreatment revealed by functional and structural magnetic resonance imaging," *Biol. Psychiatry* **71**(4), 286–293 (2012).
9. Y. W. Jun, J. H. Lee, and J. Cheon, "Chemical design of nanoparticle probes for high-performance magnetic resonance imaging," *Angew. Chem. Int. Ed. Engl.* **47**(28), 5122–5135 (2008).
10. E. Terreno et al., "Challenges for molecular magnetic resonance imaging," *Chem. Rev.* **110**(5), 3019–3042 (2010).
11. S. Martel et al., "Automatic navigation of an untethered device in the artery of a living animal using a conventional clinical magnetic resonance imaging system," *Appl. Phys. Lett.* **90**(11), 114105 (2007).
12. A. P. Slobozhanyuk et al., "Visualization of metasurface eigenmodes with magnetic resonance imaging," *Phys. Rev. Appl.* **16**(2), L021002 (2021).
13. W. R. Hendee, "Physics and applications of medical imaging," *Rev. Mod. Phys.* **71**(2), S444–S450 (1999).
14. D. L. Bihan and H. Johansen-Berg, "Diffusion MRI at 25: exploring brain tissue structure and function," *NeuroImage* **61**(2), 324–341 (2012).
15. W. Wu and K. L. Miller, "Image formation in diffusion MRI: a review of recent technical developments," *J. Magn. Reson. Imaging* **46**(3), 646–662 (2017).
16. S. Eickhoff et al., "High-resolution MRI reflects myeloarchitecture and cytoarchitecture of human cerebral cortex," *Hum. Brain Mapp.* **24**(3), 206–215 (2005).
17. J. D. Bodle et al., "High-resolution magnetic resonance imaging: an emerging tool for evaluating intracranial arterial disease," *Stroke* **44**(1), 287–292 (2013).
18. G. H. Glover, "Overview of functional magnetic resonance imaging," *Neurosurg. Clin. N. Am.* **22**(2), 133–139 (2011).
19. P. A. Bandettini, "Twenty years of functional MRI: the science and the stories," *NeuroImage* **62**(2), 575–588 (2012).
20. C. K. Kuhl, F. Träber, and H. H. Schild, "Whole-body high-field-strength (3.0-T) MR imaging in clinical practice Part I. Technical considerations and clinical applications," *Radiology* **246**(3), 675–696 (2008).
21. B. Gruber et al., "RF coils: a practical guide for nonphysicists," *J. Magn. Reson. Imaging* **48**(3), 590–604 (2018).
22. X. Yan, J. C. Gore, and W. A. Grissom, "Self-decoupled radiofrequency coils for magnetic resonance imaging," *Nat. Commun.* **9**(1), 3481 (2018).

23. D. J. Tyler et al., "Magnetic resonance imaging with ultrashort TE (UTE) pulse sequences: technical considerations," *J. Magn. Reson. Imaging* **25**(2), 279–289 (2007).
24. L. Knutsson et al., "CEST, ASL, and magnetization transfer contrast: how similar pulse sequences detect different phenomena," *Magn. Reson. Med.* **80**(4), 1320–1340 (2018).
25. E. Van Reeth et al., "Super-resolution in magnetic resonance imaging: a review," *Concepts Magn. Reson. Part A* **40A**(6), 306–325 (2012).
26. E.-S. A. El-Dahshan et al., "Computer-aided diagnosis of human brain tumor through MRI: a survey and a new algorithm," *Expert Syst. Appl.* **41**(11), 5526–5545 (2014).
27. Y. D. Xiao et al., "MRI contrast agents: classification and application [Review]," *Int. J. Mol. Med.* **38**(5), 1319–1326 (2016).
28. J. Wahsner et al., "Chemistry of MRI contrast agents: current challenges and new frontiers," *Chem. Rev.* **119**(2), 957–1057 (2019).
29. A. G. Webb, "Dielectric materials in magnetic resonance," *Concepts Magn. Reson. Part A* **38A**(4), 148–184 (2011).
30. Q. X. Yang et al., "Reducing SAR and enhancing cerebral signal-to-noise ratio with high permittivity padding at 3 T," *Magn. Reson. Med.* **65**(2), 358–362 (2011).
31. S. A. Aussenhofer and A. G. Webb, "High-permittivity solid ceramic resonators for high-field human MRI," *NMR Biomed.* **26**(11), 1555–1561 (2013).
32. A. Shchelokova et al., "Ceramic resonators for targeted clinical magnetic resonance imaging of the breast," *Nat. Commun.* **11**(1), 3840 (2020).
33. J. B. Pendry et al., "Magnetism from conductors and enhanced nonlinear phenomena," *IEEE Trans. Microw. Theory Tech.* **47**(11), 2075–2084 (1999).
34. R. A. Shelby, D. R. Smith, and S. Schultz, "Experimental verification of a negative index of refraction," *Science* **292**(5514), 77–79 (2001).
35. R. Schmidt et al., "Flexible and compact hybrid metasurfaces for enhanced ultra high field in vivo magnetic resonance imaging," *Sci. Rep.* **7**, 1678 (2017).
36. R. Schmidt and A. Webb, "Metamaterial combining electric- and magnetic-dipole-based configurations for unique dual-band signal enhancement in ultrahigh-field magnetic resonance imaging," *ACS Appl. Mater. Interfaces* **9**(40), 34618–34624 (2017).
37. A. V. Shchelokova et al., "Volumetric wireless coil based on periodically coupled split-loop resonators for clinical wrist imaging," *Magn. Reson. Med.* **80**(4), 1726–1737 (2018).
38. K. Wu et al., "Auxetics-inspired tunable metamaterials for magnetic resonance imaging," *Adv. Mater.* **34**(6), 2109032 (2022).
39. Z. Chi et al., "Adaptive cylindrical wireless metasurfaces in clinical magnetic resonance imaging," *Adv. Mater.* **33**(40), 2102469 (2021).
40. X. Zhao et al., "Intelligent metamaterials based on nonlinearity for magnetic resonance imaging," *Adv. Mater.* **31**(49), 1905461 (2019).
41. D. Schurig et al., "Metamaterial electromagnetic cloak at microwave frequencies," *Science* **314**(5801), 977–980 (2006).
42. T. Ergin et al., "Three-dimensional invisibility cloak at optical wavelengths," *Science* **328**(5976), 337–339 (2010).
43. X. Liu et al., "Infrared spatial and frequency selective metamaterial with near-unity absorbance," *Phys. Rev. Lett.* **104**(20), 207403 (2010).
44. C. M. Watts, X. Liu, and W. J. Padilla, "Metamaterial electromagnetic wave absorbers," *Adv. Mater.* **24**(23), OP98–OP120 (2012).
45. F. Lemoult et al., "Resonant metalenses for breaking the diffraction barrier," *Phys. Rev. Lett.* **104**(20), 203901 (2010).
46. M. Khorasaninejad et al., "Metalenses at visible wavelengths: diffraction-limited focusing and subwavelength resolution imaging," *Science* **352**(6290), 1190–1194 (2016).
47. C. L. Holloway et al., "A discussion on the interpretation and characterization of metafilms/metasurfaces: the two-dimensional equivalent of metamaterials," *Metamaterials* **3**(2), 100–112 (2009).
48. A. V. Kildishev, A. Boltasseva, and V. M. Shalaev, "Planar photonics with metasurfaces," *Science* **339**(6125), 1232009 (2013).
49. N. Yu and F. Capasso, "Flat optics with designer metasurfaces," *Nat. Mater.* **13**(2), 139–150 (2014).
50. J. P. Marques, F. F. J. Simonis, and A. G. Webb, "Low-field MRI: an MR physics perspective," *J. Magn. Reson. Imaging* **49**(6), 1528–1542 (2019).
51. W. J. Padilla and R. D. Averitt, "Imaging with metamaterials," *Nat. Rev. Phys.* **4**(2), 85–100 (2022).
52. P. Danhier and B. Gallez, "Electron paramagnetic resonance: a powerful tool to support magnetic resonance imaging research," *Contrast Media Mol. Imaging* **10**(4), 266–281 (2015).
53. M. H. Levitt, *Spin Dynamics: Basics of Nuclear Magnetic Resonance*, 2nd ed., Wiley, Chichester (2012).
54. M. A. Bernstein, K. F. King, and X. J. Zhou, *Handbook of MRI Pulse Sequences*, Elsevier Science, Burlington (2004).
55. R. Damadian, "Tumor detection by nuclear magnetic resonance," *Science* **171**(3976), 1151–1153 (1971).
56. R. W. Brown et al., *Magnetic Resonance Imaging: Physical Principles and Sequence Design*, 2nd ed., Wiley, Hoboken, NJ (2014).
57. C. Westbrook and J. Talbot, *MRI in Practice*, 4th ed., Wiley, Hoboken, NJ (2011).
58. C. E. Hayes et al., "An efficient, highly homogeneous radiofrequency coil for whole-body NMR imaging at 1.5 T," *J. Magn. Reson.* **63**(3), 622–628 (1985).
59. A. P. Slobozhanyuk et al., "Enhancement of magnetic resonance imaging with metasurfaces," *Adv. Mater.* **28**(9), 1832–1838 (2016).
60. D. I. Hoult, "The principle of reciprocity in signal strength calculations: a mathematical guide," *Concepts Magn. Reson.* **12**(4), 173–187 (2000).
61. M. H. Khan et al., "Short- and long-term effects of 3.5–23.0 Tesla ultra-high magnetic fields on mice behaviour," *Eur. Radiol.* **32**(8), 5596–5605 (2022).
62. J. T. Rosenberg, S. C. Grant, and D. Topgaard, "Nonparametric 5D D-R(2) distribution imaging with single-shot EPI at 21.1 T: initial results for *in vivo* rat brain," *J. Magn. Reson.* **341**, 107256 (2022).
63. Q. X. Yang et al., "Analysis of wave behavior in lossy dielectric samples at high field," *Magn. Reson. Med.* **47**(5), 982–989 (2002).
64. T. C. Choy, *Effective Medium Theory: Principles and Applications*, 2nd ed., Oxford University Press, New York (2016).
65. J. T. Vaughan et al., "High frequency volume coils for clinical NMR imaging and spectroscopy," *Magn. Reson. Med.* **32**(2), 206–218 (1994).
66. M. C. K. Wiltshire et al., "Microstructured magnetic materials for RF flux guides in magnetic resonance imaging," *Science* **291**(5505), 849–851 (2001).
67. M. C. K. Wiltshire et al., "Metamaterial endoscope for magnetic field transfer: near field imaging with magnetic wires," *Opt. Express* **11**(7), 709–715 (2003).
68. M. J. Freire et al., "On the applications of $\mu_r = -1$ metamaterial lenses for magnetic resonance imaging," *J. Magn. Reson.* **203**(1), 81–90 (2010).
69. M. A. Lopez et al., "Nonlinear split-ring metamaterial slabs for magnetic resonance imaging," *Appl. Phys. Lett.* **98**(13), 133508 (2011).
70. M. C. K. Wiltshire, "Radio frequency (RF) metamaterials," *Phys. Status Solidi B* **244**(4), 1227–1236 (2007).

71. M. Allard and R. M. Henkelman, "Using metamaterial yokes in NMR measurements," *J. Magn. Reson.* **182**(2), 200–207 (2006).
72. D. R. Smith, J. B. Pendry, and M. C. K. Wiltshire, "Metamaterials and negative refractive index," *Science* **305**(5685), 788–792 (2004).
73. S. Xi et al., "Experimental verification of reversed Cherenkov radiation in left-handed metamaterial," *Phys. Rev. Lett.* **103**(19), 194801 (2009).
74. E. J. Reed, M. Soljacic, and J. D. Joannopoulos, "Reversed Doppler effect in photonic crystals," *Phys. Rev. Lett.* **91**(13), 133901 (2003).
75. N. Fang and X. Zhang, "Imaging properties of a metamaterial superlens," *Appl. Phys. Lett.* **82**(2), 161–163 (2003).
76. J. M. Algarin et al., "Signal-to-noise ratio evaluation in resonant ring metamaterial lenses for MRI applications," *New J. Phys.* **13**(11), 115006 (2011).
77. J. M. Algarin et al., "Analysis of the resolution of split-ring metamaterial lenses with application in parallel magnetic resonance imaging," *Appl. Phys. Lett.* **98**(1), 014105 (2011).
78. D. J. Larkman and R. G. Nunes, "Parallel magnetic resonance imaging," *Phys. Med. Biol.* **52**(7), R15–R55 (2007).
79. E. Motovilova et al., "Water-tunable highly sub-wavelength spiral resonator for magnetic field enhancement of MRI coils at 1.5 T," *IEEE Access* **7**, 90304–90315 (2019).
80. E. Motovilova and S. Y. Huang, "Hilbert curve-based metasurface to enhance sensitivity of radio frequency coils for 7-T MRI," *IEEE Trans. Microw. Theory Tech.* **67**(2), 615–625 (2019).
81. P. de Heer et al., "Increasing signal homogeneity and image quality in abdominal imaging at 3 T with very high permittivity materials," *Magn. Reson. Med.* **68**(4), 1317–1324 (2012).
82. W. M. Brink and A. G. Webb, "High permittivity pads reduce specific absorption rate, improve B1 homogeneity, and increase contrast-to-noise ratio for functional cardiac MRI at 3 T," *Magn. Reson. Med.* **71**(4), 1632–1640 (2013).
83. V. Vorobyev et al., "An artificial dielectric slab for ultra high-field MRI: proof of concept," *J. Magn. Reson.* **320**, 106835 (2020).
84. V. Vorobyev et al., "Improving B_1^+ homogeneity in abdominal imaging at 3 T with light, flexible, and compact metasurface," *Magn. Reson. Med.* **87**(1), 496–508 (2021).
85. E. Shamonina et al., "Magnetoinductive waves in one, two, and three dimensions," *J. Appl. Phys.* **92**(10), 6252–6261 (2002).
86. L. Solymar et al., "Rotational resonance of magnetoinductive waves: basic concept and application to nuclear magnetic resonance," *J. Appl. Phys.* **99**(12), 123908 (2006).
87. R. R. A. Syms et al., "Flexible magnetoinductive ring MRI detector: design for invariant nearest-neighbour coupling," *Metamaterials* **4**(1), 1–14 (2010).
88. C. R. Simovski et al., "Wire metamaterials: physics and applications," *Adv. Mater.* **24**(31), 4229–4248 (2012).
89. X. Radu, D. Garray, and C. Craeye, "Toward a wire medium endoscope for MRI imaging," *Metamaterials* **3**(2), 90–99 (2009).
90. M. C. K. Wiltshire et al., "Experimental and theoretical study of magneto-inductive waves supported by one-dimensional arrays of "Swiss rolls"," *J. Appl. Phys.* **95**(8), 4488–4493 (2004).
91. R. R. A. Syms, E. Shamonina, and L. Solymar, "Magneto-inductive waveguide devices," *IEE P-Microw. Antennas Propag.* **153**(2), 111–121 (2006).
92. G. Shvets et al., "Guiding, focusing, and sensing on the subwavelength scale using metallic wire arrays," *Phys. Rev. Lett.* **99**(5), 053903 (2007).
93. P. A. Belov et al., "Enhancement of evanescent spatial harmonics inside media with extreme optical anisotropy," *Opt. Lett.* **34**(4), 527–529 (2009).
94. A. Poddubny et al., "Hyperbolic metamaterials," *Nat. Photonics* **7**(12), 948–957 (2013).
95. P. A. Belov et al., "Strong spatial dispersion in wire media in the very large wavelength limit," *Phys. Rev. B* **67**(11), 113103 (2003).
96. P. A. Belov, C. R. Simovski, and P. Ikonen, "Canalization of subwavelength images by electromagnetic crystals," *Phys. Rev. B* **71**(19), 193105 (2005).
97. P. A. Belov, Y. Hao, and S. Sudhakaran, "Subwavelength microwave imaging using an array of parallel conducting wires as a lens," *Phys. Rev. B* **73**(3), 033108 (2006).
98. X. Radu, A. Lapeyronnie, and C. Craeye, "Numerical and experimental analysis of a wire medium collimator for magnetic resonance imaging," *Electromagnetics* **28**(7), 531–543 (2008).
99. A. P. Slobozhanyuk et al., "An endoscope based on extremely anisotropic metamaterials for applications in magnetic resonance imaging," *J. Commun. Technol. Electron.* **59**(6), 562–570 (2014).
100. A. P. Slobozhanyuk et al., "Experimental verification of enhancement of evanescent waves inside a wire medium," *Appl. Phys. Lett.* **103**(5), 051118 (2013).
101. M. Dubois et al., "Kerker effect in ultrahigh-field magnetic resonance imaging," *Phys. Rev. X* **8**(3), 031083 (2018).
102. T. Itoh and C. Caloz, *Electromagnetic Metamaterials: Transmission Line Theory and Microwave Applications*, Wiley, New York (2005).
103. D. Erni et al., "Highly adaptive RF excitation scheme based on conformal resonant CRLH metamaterial ring antennas for 7-Tesla traveling-wave magnetic resonance imaging," in *Annu. Int. Conf. IEEE Eng. in Med. and Biol. Soc.*, IEEE, Boston, MA, USA, pp. 554–558 (2011).
104. H. Yang et al., "Tailored RF magnetic field distribution along the bore of a 7-Tesla traveling-wave magnetic resonance imaging system," in *Int. Conf. Electromagn. in Adv. Appl.*, IEEE, Turin, Italy, pp. 468–471 (2013).
105. C. Caloz, A. Sanada, and T. Itoh, "A novel composite right-/left-handed coupled-line directional coupler with arbitrary coupling level and broad bandwidth," *IEEE Trans. Microw. Theory Tech.* **52**(3), 980–992 (2004).
106. M. Alibakhshikenari et al., "High-gain metasurface in polyimide on-chip antenna based on CRLH-TL for sub-terahertz integrated circuits," *Sci. Rep.* **10**(1), 4298 (2020).
107. H. Lee, D. Ren, and J. H. Choi, "Dual-band and polarization-flexible CRLH substrate-integrated waveguide resonant antenna," *IEEE Antennas Wirel. Propag. Lett.* **17**(8), 1469–1472 (2018).
108. X. X. Wang et al., "Unique Huygens-Fresnel electromagnetic transportation of chiral Dirac wavelet in topological photonic crystal," *Nat. Commun.* **14**, 3040 (2023).
109. Z. Guo et al., "Anomalous broadband Floquet topological metasurface with pure site rings," *Adv. Photonics Nexus* **2**(1), 016006 (2023).
110. V. Panda et al., "A zeroth order resonant element for MRI transmission line RF coil," in *IEEE Int. Symp. Antennas and Propag.*, IEEE, Fajardo, Puerto Rico, pp. 1389–1390 (2016).
111. T. K. Truong et al., "Effects of static and radiofrequency magnetic field inhomogeneity in ultra-high field magnetic resonance imaging," *Magn. Reson. Imaging* **24**(2), 103–112 (2006).
112. V. Panda et al., "Metamaterial zeroth-order resonator RF coil for human head: preliminary design for 10.5 T MRI," *IEEE J. Electromagn. RF Microw. Med. Biol.* **3**(1), 33–40 (2019).
113. D. O. Brunner et al., "Travelling-wave nuclear magnetic resonance," *Nature* **457**(7232), 994–998 (2009).
114. T. Herrmann et al., "Metamaterial-based transmit and receive system for whole-body magnetic resonance imaging at ultra-high magnetic fields," *PLoS One* **13**(1), e0191719 (2018).
115. Y. Zeng et al., "Modal analysis method to describe weak nonlinear effects in metamaterials," *Phys. Rev. B* **85**(12), 125107 (2012).
116. A. V. Shchelokova et al., "Experimental investigation of a metasurface resonator for in vivo imaging at 1.5 T," *J. Magn. Reson.* **286**, 78–81 (2018).

117. E. Brui et al., "Volumetric wireless coil for wrist MRI at 1.5 T as a practical alternative to Tx/Rx extremity coil: a comparative study," *J. Magn. Reson.* **339**, 107209 (2022).
118. E. A. Brui et al., "Adjustable subwavelength metasurface-inspired resonator for magnetic resonance imaging," *Phys. Status Solidi A* **215**(5), 1700788 (2018).
119. A. Hurshkainen et al., "A novel metamaterial-inspired RF-coil for preclinical dual-nuclei MRI," *Sci. Rep.* **8**(1), 9190 (2018).
120. G. Duan et al., "Boosting magnetic resonance imaging signal-to-noise ratio using magnetic metamaterials," *Commun. Phys.* **2**(1), 35 (2019).
121. P. Das et al., "A thin metallo-dielectric stacked metamaterial as "add-on" for magnetic field enhancement in clinical MRI," *J. Appl. Phys.* **132**(11), 114901 (2022).
122. V. Puchnin et al., "Metamaterial inspired wireless coil for clinical breast imaging," *J. Magn. Reson.* **322**, 106877 (2021).
123. S. Maslovski et al., "Artificial magnetic materials based on the new magnetic particle: metasolenoid," *Prog. Electromagn. Res.* **54**, 61–81 (2005).
124. L. Nohava et al., "Perspectives in wireless radio frequency coil development for magnetic resonance imaging," *Front. Phys.* **8**, 11 (2020).
125. V. M. Puchnin et al., "Application of topological edge states in magnetic resonance imaging," *Phys. Rev. Appl.* **20**(2), 024076 (2023).
126. A. V. Shchelokova et al., "Locally enhanced image quality with tunable hybrid metasurfaces," *Phys. Rev. Appl.* **9**(1), 014020 (2018).
127. E. I. Kretov, A. V. Shchelokova, and A. P. Slobozhanyuk, "Control of the magnetic near-field pattern inside MRI machine with tunable metasurface," *Appl. Phys. Lett.* **115**(6), 061604 (2019).
128. H. Wang et al., "On-demand field shaping for enhanced magnetic resonance imaging using an ultrathin reconfigurable metasurface," *View* **2**(3), 20200099 (2021).
129. A. Jandaliyeva et al., "Control of the near magnetic field pattern uniformity inside metamaterial-inspired volumetric resonators," *Photonics Nanostruct.* **48**, 100989 (2022).
130. E. I. Kretov, A. V. Shchelokova, and A. P. Slobozhanyuk, "Impact of wire metasurface eigenmode on the sensitivity enhancement of MRI system," *Appl. Phys. Lett.* **112**(3), 033501 (2018).
131. S. Zhang et al., "Recent advances in nonlinear optics for bio-imaging applications," *Opto-Electron. Adv.* **3**(10), 200003 (2020).
132. E. Stoja et al., "Improving magnetic resonance imaging with smart and thin metasurfaces," *Sci. Rep.* **11**(1), 16179 (2021).
133. S. Saha et al., "A smart switching system to enable automatic tuning and detuning of metamaterial resonators in MRI scans," *Sci. Rep.* **10**(1), 10042 (2020).
134. I. Liberal and N. Engheta, "Near-zero refractive index photonics," *Nat. Photonics* **11**(3), 149–158 (2017).
135. Y. Chen et al., "Experimental demonstration of the magnetic field concentration effect in circuit-based magnetic near-zero index media," *Opt. Express* **28**(11), 17064–17075 (2020).
136. D. Lee et al., "Hyperbolic metamaterials: fusing artificial structures to natural 2D materials," *eLight* **2**, 1 (2022).
137. Y. Wang et al., "Circuit-based magnetic hyperbolic cavities," *Phys. Rev. Appl.* **13**(4), 044024 (2020).
138. X. Yang et al., "Experimental realization of three-dimensional indefinite cavities at the nanoscale with anomalous scaling laws," *Nat. Photonics* **6**(7), 450–454 (2012).
139. Z. Guo, H. Jiang, and H. Chen, "Zero-index and hyperbolic metacavities: fundamentals and applications," *J. Phys. D: Appl. Phys.* **55**(8), 083001 (2021).
140. N. I. Zheludev and Y. S. Kivshar, "From metamaterials to metadevices," *Nat. Mater.* **11**(11), 917–924 (2012).
141. T. J. Cui et al., "Coding metamaterials, digital metamaterials and programmable metamaterials," *Light: Sci. Appl.* **3**(10), e218 (2014).
142. A. S. Lundervold and A. Lundervold, "An overview of deep learning in medical imaging focusing on MRI," *Z. Med. Phys.* **29**(2), 102–127 (2019).
143. M. Song et al., "Multi-mode metamaterial-inspired resonator for near-field wireless power transfer," *Appl. Phys. Lett.* **117**(8), 083501 (2020).
144. Z. Guo et al., "Level pinning of anti-PT-symmetric circuits for efficient wireless power transfer," *Nat. Sci. Rev.* **11**(1), nwad172 (2024).

Zhiwei Guo received his PhD in physics from Tongji University, Shanghai, China, in 2019. Currently, he is an associate professor in the School of Physics Science and Engineering at Tongji University. His current research interests include non-Hermitian photonics, topological photonics, circuit-based metamaterials, photonic crystals with metamaterials, metasources for near-field routing, and wireless power transfer.

Yang Xu received his BSc degree from Tongji University, Shanghai, China, in 2019, where he is currently pursuing a PhD in physics at the School of Physics Science and Engineering. His research interests include magnetic resonance imaging, zero-index metamaterials, and moiré metamaterials.

Hong Chen is a distinguished professor in the School of Physics Science and Engineering at Tongji University, Shanghai, China. He received his BSc degree in physics from Fudan University, Shanghai, China, in 1982 and his PhD in condensed matter physics from Shanghai Jiaotong University, Shanghai, China, in 1986. His research interests include photonic crystals, metamaterials, plasmonics, and artificial microstructures for manipulation of classical and quantum waves.

Biographies of the other authors are not available.